arXiv:2301.09313v1 [cond-mat.mtrl-sci] 23 Jan 2023

Graphical Abstract

Two-stage 2D-to-3D reconstruction of realistic microstructures: Implementation and numerical validation by effective properties

Paul Seibert,Alexander Raßloff,Karl A. Kalina,Joachim Gussone,Katrin Bugelnig,Martin Diehl,Markus Kästner

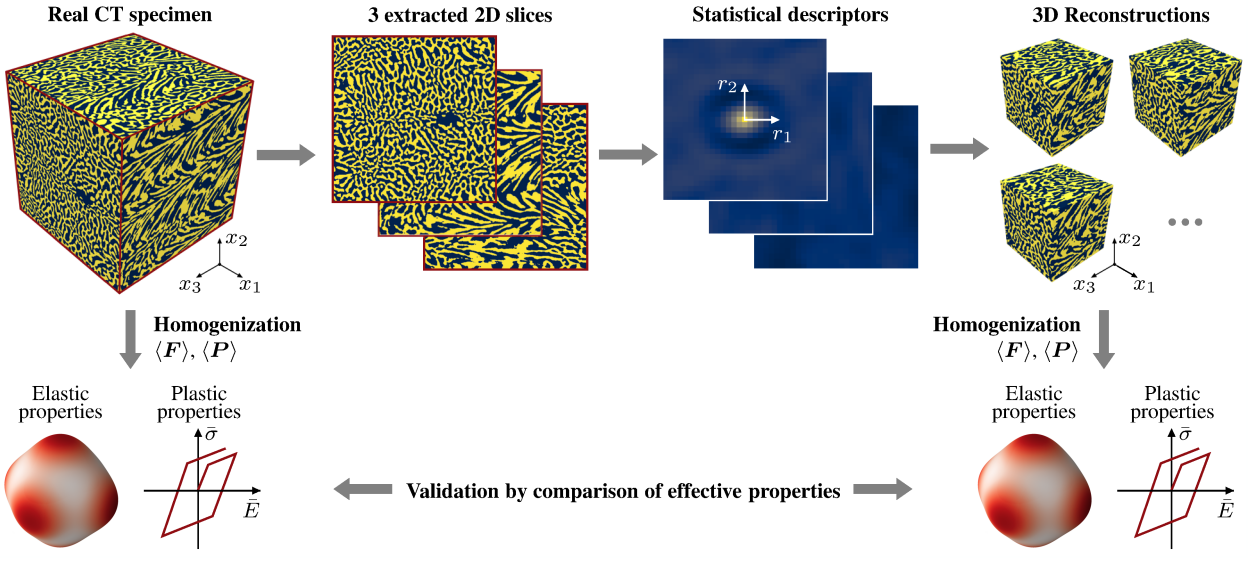

Highlights

Two-stage 2D-to-3D reconstruction of realistic microstructures: Implementation and numerical validation by effective properties

Paul Seibert,Alexander Raßloff,Karl A. Kalina,Joachim Gussone,Katrin Bugelnig,Martin Diehl,Markus Kästner

- Two-stage gradient-based algorithm for reconstructing realistic 3D microstructures from 2D slices
- Validation based on real computed tomography scan of recent Ti-Fe system and synthetic spinodoid structures
- Error analysis in terms of statistical descriptors as well as simulated anisotropic elastic and plastic effective behavior

Two-stage 2D-to-3D reconstruction of realistic microstructures: Implementation and numerical validation by effective properties

Paul Seibert[a], Alexander Raßloff[a], Karl A. Kalina[a], Joachim Gussone[b], Katrin Bugelnig[b], Martin Diehl[c,d] and Markus Kästner[a,e,*]

[a]Institute of Solid Mechanics, TU Dresden, Dresden, 01069, Germany
[b]Institute of Materials Research, German Aerospace Center (DLR), Lindner Hoehe, Cologne, 51147, Germany
[c]Department of Computer Science, KU Leuven, Celestijnenlaan 200A, Leuven, 3001, Belgium
[d]Department of Materials Engineering, KU Leuven, Kasteelpark Arenberg 44, Leuven, 3001, Belgium
[e]Dresden Center for Computational Materials Science, TU Dresden, Dresden, 01069, Germany

ARTICLE INFO

Keywords:
microstructure
characterization
reconstruction
differentiable
descriptor
random heterogeneous media

ABSTRACT

Realistic microscale domains are an essential step towards making modern multiscale simulations more applicable to computational materials engineering. For this purpose, 3D computed tomography scans can be very expensive or technically impossible for certain materials, whereas 2D information can be easier obtained. Based on a single or three orthogonal 2D slices, the recently proposed differentiable microstructure characterization and reconstruction (DMCR) algorithm is able to reconstruct multiple plausible 3D realizations of the microstructure based on statistical descriptors, i.e., without the need for a training data set. Building upon DMCR, this work introduces a highly accurate two-stage reconstruction algorithm that refines the DMCR results under consideration of microstructure descriptors. Furthermore, the 2D-to-3D reconstruction is validated using a real computed tomography (CT) scan of a recently developed β-Ti/TiFe alloy as well as anisotropic "bone-like" spinodoid structures. After a detailed discussion of systematic errors in the descriptor space, the reconstructed microstructures are compared to the reference in terms of the numerically obtained effective elastic and plastic properties. Together with the free accessibility of the presented algorithms in *MCRpy*, the excellent results in this study motivate interdisciplinary cooperation in applying numerical multiscale simulations for computational materials engineering.

1. Introduction

Computational micromechanics has experienced significant progress in the last decade. Fast multiscale schemes [34, 35, 16, 40, 28] alleviate the computational burden of FE^2 (finite element square). Based on the fast Fourier transform (FFT), efficient approaches have been presented for the homogenization of the effective behavior of heterogeneous media [42] or for simulation using composite voxels [27, 54, 55, 31]. Furthermore, fast surrogates for the computationally intensive homogenization are given by convolutional neural networks [60, 13, 23] or deep material networks [37, 38, 17] trained on the basis of suitable data sets. In summary, extensive research is conducted on the constitutive and multiscale aspects of computational micromechanics, with a focus on high accuracy or performance. In contrast, a very relevant field that attracts relatively little attention is the generation of realistic 3D volume elements, especially if these are solely based on 2D image data [2]. While special cases like fiber composites have relatively well-defined microscale geometries, many engineering materials are random heterogeneous media. For these complex materials, the elastic [64] and plastic [63] behavior can be very sensitive[1] to the exact 3D micro-geometry [11, 10], which is, however, stochastic and unknown. Computed tomography (CT) scans are a common strategy for directly obtaining this 3D information [3]. However, compared to microscopy images, CT scans require intricate computer post-processing, where the chosen parameters of filters and thresholds strongly influence the microstructure and the predicted material behavior [18]. Furthermore, for some materials and length scales, CT scans are either very

*Corresponding author
ORCID(s): 0000-0002-8774-8462 (P. Seibert); 0000-0002-9134-4874 (A. Raßloff); 0000-0001-6170-4069 (K.A. Kalina); 0000-0002-3036-5188 (J. Gussone); 0000-0003-0932-1751 (K. Bugelnig); 0000-0002-3738-7363 (M. Diehl); 0000-0003-3358-1545 (M. Kästner)

[1]For instance, determining yield surfaces by virtual testing is a relevant and open problem [19, 22] with ongoing developments [32, 66, 43].

expensive [21] or technically impossible due to a lack of phase contrast. The alternative, serial sectioning, becomes extremely expensive and time-consuming. In contrast, obtaining microscopy images of one or few cross-sections can be significantly more feasible and requires fewer impactful parameters to be chosen manually. These images can serve as a 2D basis for the reconstruction of 3D microstructures.

A brief introduction on microstructure reconstruction techniques with a focus on recent techniques for random heterogeneous media is given in the following. For this purpose, a distinction is made between *descriptor-based* and *data-based* methods. The reader is referred to the reviews [2, 5, 50] for a more detailed overview.

Inspired from the advent of machine learning, data-based methods have received much attention lately. The central idea is to train a generative machine learning model on a data set of microstructures[2] and to then use the trained model to sample new realizations of the same structure. Noticeable examples are generative adversarial networks for 2D-to-3D [30] and 3D-to-3D [24] reconstruction as well as hybrid methods with autoencoders [65] or transformers [47]. While these methods achieve excellent results throughout a variety of material classes, the disadvantage of data-based methods is the general necessity of a data set.

Descriptor-based methods, in contrast, do not require a training data set. Instead of training a generative machine learning model by optimizing its weights, the optimization problem is directly carried out in the space of possible microstructures. For this purpose, the utility of a microstructure is computed by means of a descriptor that quantifies the morphology of the structure. These descriptors can range from simple volume fractions to high-dimensional n-point statistics and are discussed in more detail in Section 2.1. The desired value of the descriptor can be prescribed directly or computed from a reference microstructure. Here, a *single* microstructure example is sufficient for descriptor-based reconstruction, as opposed to machine learning methods, which usually require a data *set* of structures. While the latter need data to learn how to constrain their own flexibility, the former harness expert knowledge about microstructure descriptors to reduce the required amount of data to a minimum. One of the most well-known descriptor-based reconstruction methods is the Yeong-Torquato algorithm [62], which directly solves the optimization problem using a specially adapted version of a common stochastic optimizer. While this is very elegant, it becomes computationally challenging at high resolutions and in 3D, where billions of iterations are required for convergence [1]. A common method of simplifying the optimization problem is to approximate the structure by ellipsoidal [61, 51] inclusions or by directly incorporating the grain structure of metallic materials [20]. Alternatively, without any approximations on the microstructure morphology, *differentiable* descriptors can be used in order to directly solve the underlying optimization problem using a gradient based optimizer. This is known as differentiable microstructure characterization and reconstruction (DMCR) [56, 57] and has been made publicly available by the authors in the *MCRpy* package [58].

Based on this work, the present contribution proposes a two-stage reconstruction algorithm that improves upon DMCR by (i) guaranteeing the correct volume fractions and (ii) producing smoother results without introducing descriptor discrepancies. With DMCR constituting the first stage, the need for a descriptor-based smoothing procedure is stressed and the implementation of this post-processing step is discussed in detail. Furthermore, the aim of this work is to rigorously validate the reconstruction procedure, i.e., to systematically check for the physical plausibility of 3D microstructures reconstructed from one or few 2D slices. Thereby, a special feature of this contribution is to use real 3D CT data of a novel titanium alloy that was developed for additive manufacturing [21] as a reference, which shows a much higher morphological complexity than common synthetic structures. For this, a single slice is extracted from the 3D data to mimic the case that only a 2D microscopy image is available. The reconstruction from this slice is compared to the original 3D data regarding (i) the microstructure morphology, quantified by statistical descriptors, and (ii) the simulated and homogenized elastic and plastic properties. Using the homogenized properties, the same procedure is repeated on a higher length scale for synthetic spinodoid "bone-like" metamaterials [33] to apply the algorithm in the highly anisotropic regime. While some previous works on microstructure reconstruction list errors for the Young's modulus [9, 24], to the authors' best knowledge, the present work is the first to (i) consider the full anisotropic stiffness tensor, (ii) also determine the plastic response and (iii) validate a reconstruction procedure based on DMCR. Overall, the present work not only proposes a new microstructure reconstruction workflow, but also aims at demonstrating its range of applicability, allowing the multiscale modeling and simulation community to assess its potential. This creates a basis for a plethora of possible future works that harness both, microstructure reconstruction and numerical homogenization, to advance scale-bridging simulations of complex materials.

[2] Sometimes, a single, very large microstructure is used and split into smaller sections or cut into slices. However, it could be argued that this is more similar to starting with a set of training data than to really requiring a single example only.

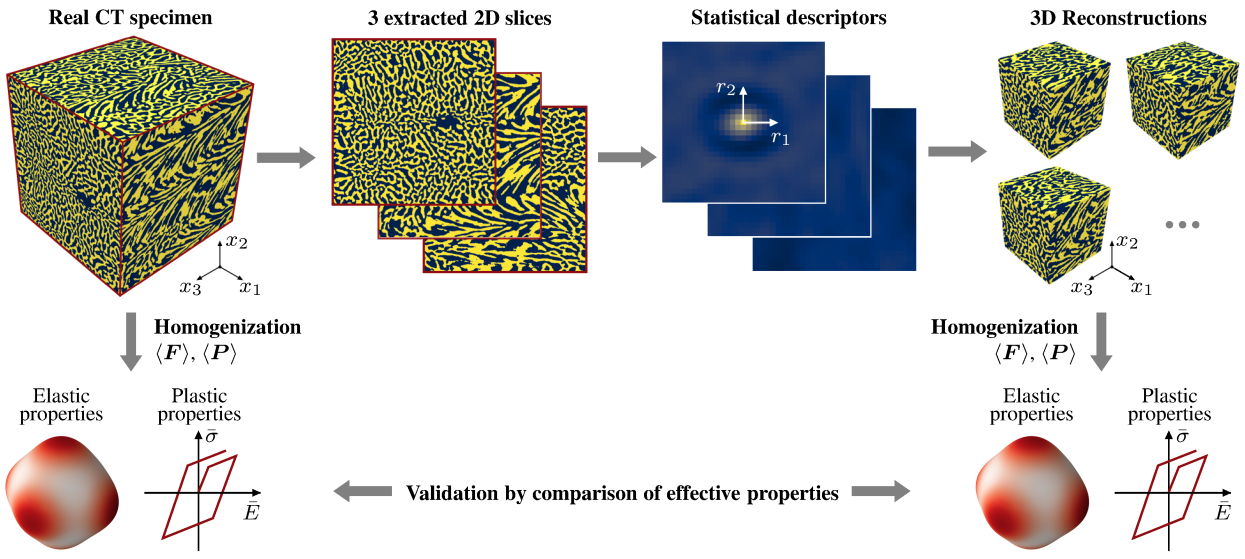

Figure 1: Schematic overview of the validation procedure: Three orthogonal slices are extracted from a real 3D specimen to mimic the situation that only 2D data is available. From these slices, multiple synthetic structures are reconstructed based on statistical descriptors and compared to the reference in terms of morphology as well as the effective elastic and plastic response. Herein, r_1 and r_2 denote the coordinates of the vector $\boldsymbol{r}$ for the computation of the spatial two-point correlation.

The organization of the paper is as follows: After an introduction to the underlying methods in Section 2, the experimental and synthetic 3D data used for validation are presented in Section 3. The results are presented and discussed in Section 4 and a conclusion is drawn in Section 5.

The notation within this work is as follows: Tensors of first and second order are denoted as bold and italic letters in lower and uppercase, i.e., $\boldsymbol{a}$ and $\boldsymbol{A}$, respectively. Furthermore, fourth-order tensors are given by $\mathbb{A}$. Single and double contractions of tensors are denoted by $\boldsymbol{A} \cdot \boldsymbol{B}$ and $\boldsymbol{A} : \boldsymbol{B}$, respectively. Arrays, in contrast, are bold but not italic, i.e., $\mathbf{A}$, and the dimension is generally not specified. The coordinates of a tensor are given by $[A_{kl}]$, whereas the entries of an array are given by $A_{i,j,k}$. This allows to simply express the i-th slice in the first dimension of an array as $\mathbf{A}_{i,:,:}$. More detail on this notation is given in Section 2.2. The Einstein summation convention is not used.

2. Methods

In this work, 2D-to-3D microstructure reconstruction is numerically validated as shown in Figure 1: From a 3D reference microstructure, three orthogonal slices are extracted. These slices are characterized by statistical descriptors as described in Section 2.1. Based on these descriptors, multiple 3D realizations of the structure are reconstructed using a new, two-stage procedure. With DMCR as a first step being introduced in Section 2.2, a descriptor-based post-processing and smoothing is presented in Section 2.3 as a second step. In Section 2.4, the reconstructed structures serve as volume elements for computational homogenization in order to obtain the effective elasto-plastic properties. These values are compared to the material response of the original 3D data in order to quantify the reconstruction error.

2.1. Microstructure Characterization

The characterization function

$$f_C : \mathbf{M} \mapsto \{\mathbf{D}_i\}_{i=1}^{n_\mathrm{d}} \tag{1}$$

maps the pixel- or voxel-based representation of a microstructure $\mathbf{M}$ to a set of n_d different descriptors $\mathbf{D}_i$. These descriptors quantify the microstructure morphology in a stationary and translation-invariant manner. This allows for quantitative comparisons of microstructures, for example the computation of differences. Volume fractions and

pore size distributions are simple examples of such descriptors, however, in this work, more abstract and high-dimensional descriptors are employed. Specifically, we use spatial three-point correlations, Gram matrices of the VGG-19 network [59] and the variation descriptor as laid out in the following.

2.1.1. Spatial Correlations

Spatial n-point correlations are one of the most commonly used descriptors for random heterogeneous media [62, 5]. An excellent introduction is given in [26] and briefly summarized in the following. Consider an indicator function

$$I^p(\boldsymbol{x}) = \begin{cases} 1 & , \text{ if } \boldsymbol{x} \in V_p \\ 0 & , \text{ else} \end{cases} \tag{2}$$

of the spatial coordinates $\boldsymbol{x}$, where V_p is the region occupied by phase p. Spatial n-point correlations stochastically quantify the outcome of simultaneously probing this indicator function at different spatial locations $(\boldsymbol{x}^1, \boldsymbol{x}^2, ..., \boldsymbol{x}^n)$. Considering only statistically homogeneous media, the n-point correlation function does not depend on the absolute positions, but only their relative displacements $\boldsymbol{r}^{ij} = \boldsymbol{x}^j - \boldsymbol{x}^i$. Thus, the n-point correlation function of phases $p_1, p_2, ..., p_m$ can then be written as[3]

$$S_n^{p_1,p_2,...,p_m}(\boldsymbol{r}^{12}, \boldsymbol{r}^{13}, ..., \boldsymbol{r}^{1n}) = \lim_{n_\mathrm{r}\to\infty} \langle I^{p_1}(\boldsymbol{x}^1)\, I^{p_2}(\boldsymbol{x}^2) \dots I^{p_n}(\boldsymbol{x}^n) \rangle^{n_\mathrm{r}}, \tag{3}$$

where the $\langle ... \rangle^{n_\mathrm{r}}$ denotes the average over an ensemble of n_r realizations of placing $\boldsymbol{x}^1$ randomly in the microstructure such that $\boldsymbol{x}^2 \dots \boldsymbol{x}^n$ follow from $\boldsymbol{x}^1$ via $(\boldsymbol{r}^{12} \dots \boldsymbol{r}^{1n})$. The special case of all phases being equal ($p_1 = p_2 = .. = p_m = p$) is called auto-correlations and is given in a simplified notation as

$$S_n^{p\to p}(\boldsymbol{r}^{12}, \boldsymbol{r}^{13}, ..., \boldsymbol{r}^{1n}) = S_n^{p,p,...,p}(\boldsymbol{r}^{12}, \boldsymbol{r}^{13}, ..., \boldsymbol{r}^{1n}) \,. \tag{4}$$

For example, the spatial two-point autocorrelation function $S_2^{1\to1}(\boldsymbol{r}^{12})$ can be interpreted as the probability of both ends of the vector $\boldsymbol{r}^{12}$ being in phase 1 when randomly placed into the microstructure. While most applications focus on S_2 only and ignore higher-order correlations for computational efficiency [6], a differentiable formulation of spatial two- and three-point correlations are given in [56] and implemented in *MCRpy* [58]. The higher computational effort is compensated by the higher information content and differentiability, which allow for an efficient reconstruction. In the following, the notation $\mathbf{S}(\mathbf{M})$ refers to an array comprising the values of $S_3^{1\to1}(\boldsymbol{r}^{12}, \boldsymbol{r}^{13})$ for the microstructure $\mathbf{M}$, where each array entry corresponds to distinct values of $\boldsymbol{r}^{12}$ and $\boldsymbol{r}^{13}$ as described in [56].

2.1.2. Gram Matrices

Gram matrices are a recent alternative approach to characterizing microstructures using the internal activations of a pre-trained convolutional neural network (CNN), which are often called feature maps [39]. The activation of the p-th channel in layer n at spatial position s is denoted as $F^n_{s,p}$. In each layer n, the activations of all channels at all positions must contain relevant information about the image, because otherwise the classification head of the network would have no basis for its predictions. These feature maps provide a richer representation than the image because each layer combines low-level features to obtain condensed, higher-order information. To harness this representation, it is rendered approximately translation-invariant by computing the Gram matrix

$$G^n_{p,r} = \sum_s F^n_{s,p} F^n_{s,r} \,. \tag{5}$$

It can be seen that the summation eliminates the spatial index s, and an analogy between the Gram matrices and spatial three-point correlations of feature maps is drawn in [56]. Gram matrices are used for microstructure classification in [39] and for reconstruction in [36, 4, 57, 58].

2.1.3. Variation

The variation was originally introduced to microstructure reconstruction as a denoising parameter [4]. The total variation accumulates the absolute deviations between neighboring pixels over the entire microstructure. Later, it was

[3] While these equation serve as a concise and comprehensive definition, FFT-based algorithms are often used in practice to efficiently compute spatial correlations [6].

shown that the normalized total variation, referred to as variation $\mathcal{V}$ in the following, can be interpreted as a conventional microstructure descriptor quantifying the amount of phase boundary per unit volume [57]. Incorporating the variation to the loss function drastically reduces noise, especially in 3D reconstruction [4, 57].

With the correlations $\mathbf{S}$, the Gram matrices $\mathbf{G}$ and the variation $\mathcal{V}$ computed on three orthogonal 2D slices, a 3D microstructure is reconstructed as described in the following section.

2.2. Gradient-based Microstructure Reconstruction

Differentiable microstructure characterization and reconstruction (DMCR) constitutes the first step in generating microstructures from the descriptors in Section 2.1. In contrast to other reconstruction frameworks like the Yeong-Torquato Algorithm [62], DMCR formulates microstructure reconstruction as a *differentiable* optimization problem, facilitating significant speedups by means of highly efficient, gradient-based optimizers. DMCR is implemented in the open-source software package *MCRpy* [58], which is used in this work. While the reader is referred to [56, 57] for a detailed description to DMCR, a brief summary is given in the following. For this purpose, the procedure is first introduced in 2D in order to define the 3D process as a composition of parallel and coupled 2D reconstructions.

2.2.1. DMCR - 2D Reconstruction

In 2D, microstructure reconstruction is approached by solving an optimization problem

$$\mathbf{M}^{\mathrm{rec}} = \underset{\mathbf{M} \in \mathcal{M}^{2\mathrm{D}}}{\arg\min}\ \mathcal{L}\left(\left\{(\mathbf{D}_i(\mathbf{M}),\ \mathbf{D}_i^{\mathrm{des}})\right\}_{i=1}^{n_{\mathrm{d}}}\right) \text{ with} \tag{6}$$

$$\mathcal{M}^{2\mathrm{D}} := \left\{\mathbf{m} \in \mathbb{R}^{N_1 \times N_2} \mid \forall i \in \{1, 2, \dots, N_1\}, j \in \{1, 2, \dots, N_2\}\ 0 \leq m_{i,j} \leq 1\right\}\ , \tag{7}$$

where the loss $\mathcal{L}$ quantifies the difference between the desired descriptor $\mathbf{D}^{\mathrm{des}}$ and its current value $\mathbf{D}(\mathbf{M})$. For example, the present results are achieved with the loss function

$$\mathcal{L}(\mathbf{M}) = \lambda_S ||\mathbf{S}(\mathbf{M}) - \mathbf{S}^{\mathrm{des}}||_{\mathrm{MSE}} + \lambda_G ||\mathbf{G}(\mathbf{M}) - \mathbf{G}^{\mathrm{des}}||_{\mathrm{MSE}} + \lambda_{\mathcal{V}} ||\mathcal{V}(\mathbf{M}) - \mathcal{V}^{\mathrm{des}}||_{\mathrm{MSE}} \tag{8}$$

where λ_S, λ_G and $\lambda_{\mathcal{V}}$ are scalar weights for the spatial correlations $\mathbf{S}$, the Gram matrices $\mathbf{G}$ and the variation $\mathcal{V}$, respectively and $||\mathbf{A}||_{\mathrm{MSE}}$ is the mean squared error norm of an array $\mathbf{A}$, i.e. the average of the squared values of all entries. In this context, it is worth noting that the search space $\mathcal{M}^{2\mathrm{D}}$ of DMCR defined in Eq. 7 not only contains integer-valued microstructures as in the Yeong-Torquato algorithm, but also real-valued "intermediate states". The reason for this choice is rooted in the gradient-based optimization of Eq. 6. In other words, while the Yeong-Torquato algorithm updates the microstructure in every iteration by applying a random mutation, DMCR utilizes the gradient $\partial_{\mathbf{M}}\mathcal{L}$ of the loss function $\mathcal{L}$ with respect to the microstructure $\mathbf{M}$ for a more informed modification of the microstructure. The existence of this gradient is ensured by using only differentiable descriptors to compose the loss function. In practical application, this requires

(i) the descriptors to be defined not only for integer-valued indicator functions, but also for real-valued "intermediate states",

(ii) the value of the descriptor not to jump discontinuously as the value of individual pixels in the microstructure gradually change, and

(iii) in order to avoid plateaus during optimization, the gradient of the descriptor is required to be non-zero for the widest possible range of arguments.

More details on the theoretical foundations of defining differentiable descriptors as well as a practical example for spatial correlations are given in [56]. Despite the constraint of differentiability, the range of possible descriptors to choose from is still very large and currently far from fully exploited [58]. Most importantly, the gradient-based optimizers that can be accessed by DMCR significantly outperform the previously used stochastic methods, reducing the number of required iterations by several orders of magnitude.

2.2.2. DMCR - 3D Reconstruction

In 3D, Eq. (8) is called on all possible 2D slices in all directions. To express this, we introduce the notation $\mathbf{M}_{i,:,:} \in \mathcal{M}^{2\mathrm{D}}$ to refer to the i-th slice in the x_1-direction of the 3D microstructure array $\mathbf{M} \in \mathcal{M}^{3\mathrm{D}}$, where $\mathcal{M}^{3\mathrm{D}} \subsetneq \mathbb{R}^{N_1 \times N_2 \times N_3}$ is the space of two-phase 3D microstructures in analogy to Eq. (7). Similarly, $\mathbf{M}_{:,j,:} \in \mathcal{M}^{2\mathrm{D}}$ and $\mathbf{M}_{:,:,k} \in \mathcal{M}^{2\mathrm{D}}$ denote the j-th and k-th slice in x_2 and x_3, respectively. Furthermore, for anisotropic structures, the

Table 1
Settings for the microstructure reconstruction using *MCRpy* [58].

Parameter	Value
Resolution	128^3
Optimizer	L-BFGS-B
Multiphase descriptors	False
Multigrid reconstruction	True
Iterations per multigrid level	800
Descriptors	$\mathbf{S}, \mathbf{G}, \mathcal{V}$
Descriptor weights	$0.1, 0.1, 10$
Correlation limit	16

desired descriptor values differ between orthogonal slices, for example $\mathbf{S}^{\text{des},x_1} \neq \mathbf{S}^{\text{des},x_2} \neq \mathbf{S}^{\text{des},x_3}$. This is accounted for by introducing different loss functions $\mathcal{L}^{x_1}$, $\mathcal{L}^{x_2}$ and $\mathcal{L}^{x_3}$ for different dimensions. With this notation, 3D reconstruction is expressed as

$$\mathbf{M}^{\text{rec}} = \underset{\mathbf{M} \in \mathcal{M}^{3\text{D}}}{\arg\min} \sum_i \mathcal{L}^{x_1}(\mathbf{M}_{i,:,:}) + \sum_j \mathcal{L}^{x_2}(\mathbf{M}_{:,j,:}) + \sum_k \mathcal{L}^{x_3}(\mathbf{M}_{:,:,k}) \, . \tag{9}$$

2.2.3. MCRpy Software Tool

MCRpy allows to compose loss functions like Eq. (8) by choosing the type of loss function and providing a list of descriptors and corresponding weights. If all descriptors are differentiable, automatic differentiation allows to use gradient-based optimizers such as L-BFGS-B [7] for the reconstruction. Furthermore, a simple multi-grid procedure is implemented that can be applied to any descriptor, where a low-resolution approximation to $\mathbf{M}$ is first computed on a coarse grid and then iteratively refined in a multi-level hierarchical pyramid scheme similar to [46, 29]. The present work uses the current version of *MCRpy* with the settings given in Table 1.

2.3. Microstructure Post-Processing

2.3.1. Motivation for Specialized Algorithm

Despite the effort of reducing noise in reconstructed structures by means of the total variation [4, 57], the reconstructed structures are still noticeably less smooth than the original one. This motivates the second step of the two-stage procedure, namely a post-processing algorithm that can reduce spurious noise while at the same time keep the descriptors associated with the structure at the desired values. This is especially relevant when investigating the effective plastic behavior of the reconstructed structures: If a post-processing procedure eliminates sharp corners that are actually observed in the real structure, this reduces the intensity of stress concentrations and consequently increases the effective yield strength. Because simple, conventional smoothing procedures such as Gaussian filters fail at distinguishing between real and spurious corners and edges, this issue requires further attention. Although a variety of smoothing algorithms have been developed [15] and their applicability to reconstructed microstructures has not been studies thoroughly yet, descriptor-based microstructure reconstruction constitutes a special case as morphological information for distinguishing between real and spurious corners is available in form of the descriptors.

2.3.2. Proposed Post-Processing

In order to make use of this information, we propose Algorithm 1: First, the reconstructed microstructure $\mathbf{M}^{\text{rec}} \in \mathcal{M}^{3\text{D}}$ is projected to $\hat{\mathbf{M}} \in \hat{\mathcal{M}}^{3\text{D}}$ by element-wise rounding, where $\hat{\mathcal{M}}^{3\text{D}} \subsetneq \mathcal{M}^{3\text{D}}$ is the set of integer-valued 3D microstructures

$$\hat{\mathcal{M}}^{3\text{D}} := \left\{ \mathbf{m} \in \mathbb{Z}^{N_1 \times N_2 \times N_3} \mid \forall i \in \{1, 2, \dots, N_1\}, j \in \{1, 2, \dots, N_2\}, k \in \{1, 2, \dots, N_3\} \, m_{i,j,k} \in \{0, 1\} \right\} \, . \tag{10}$$

Secondly, the structure is adjusted to the correct volume fraction by selecting random pixels from an over-represented phase and swapping them to under-represented phases. Thirdly, randomly selected pixels from different phases are swapped if, and only if, this reduces the error in terms of the desired descriptor. Hereby, the error is identical to the loss function (8) used during gradient-based reconstruction in Section 2.2. Most importantly, in the second and third stage of the algorithm, the probability of selecting a pixels depends on the number of neighboring pixels are of a

different phase. For this purpose, a sparse operator $P_{i,j,k,l}$ is introduced that maps microstructure entries from a triple index (i, j, k) to a single index l as

$$\hat{m}'_l = \sum_{i,j,k} P_{i,j,k,l} \hat{M}_{i,j,k} \ . \tag{11}$$

With this, the probability of selecting index l is defined as

$$p(l) \propto \max\left(0, \sum_{\tilde{l} \in \mathcal{N}(l)} \left[1 - |\hat{m}'_l - \hat{m}'_{\tilde{l}}|\right] - c\right)^2 \ , \tag{12}$$

where $\mathcal{N}(l)$ yields the six indices of the non-diagonal neighbors of l and c is a hyperparameter which is chosen as $c = 2.9$. This means that isolated pixels such as spurious noise or valid sharp corners are significantly more likely to be swapped than pixels within a phase cluster. At the same time, the zero-tolerance in the acceptance criterion ensures that valid corners are not smoothed.

Algorithm 1: Descriptor-based post-processing and smoothing procedure.

Input: Reconstructed microstructure $\mathbf{M}^{\text{rec}}$; desired volume fractions $v_{\text{f}}^{\text{des}}$; number of iterations $n_{\text{iter}}^{\max}$

$\hat{\mathbf{M}}^{\text{prev}}, v_{\text{f}}^{\text{prev}}, n_{\text{iter}} \leftarrow \hat{\mathbf{M}}^{\text{rec}}, -1, 0$ `// initialize values`

$\hat{\mathbf{M}}^{\text{rec}} \leftarrow$ projection of $\mathbf{M}^{\text{rec}}$ to $\hat{\mathbf{M}}^{\text{rec}} \in \hat{\mathbf{M}}^{\text{3D}}$ `// first step: projection`

while $|v_{\text{f}}(\hat{\mathbf{M}}^{\text{rec}}) - v_{\text{f}}^{\text{des}}| < |v_{\text{f}}^{\text{prev}} - v_{\text{f}}^{\text{des}}|$ **do** `// second step: fix volume fractions`

- $l \leftarrow$ sample index of over-represented phase with different-phase neighbors `// use Eq. (12)`
- $v_{\text{f}}^{\text{prev}}, \hat{\mathbf{M}}^{\text{prev}} \leftarrow v_{\text{f}}(\hat{\mathbf{M}}^{\text{rec}}), \hat{\mathbf{M}}^{\text{rec}}$ `// store variables`
- $\hat{\mathbf{M}}^{\text{rec}} \leftarrow$ mutation of $\hat{\mathbf{M}}^{\text{rec}}$ with value at location l flipped

end

$\hat{\mathbf{M}}^{\text{rec}} \leftarrow \hat{\mathbf{M}}^{\text{prev}}$ `// use penultimate state due to loop break criterion`

while $n_{\text{iter}} \leq n_{\text{iter}}^{\max}$ **do** `// third step: smooth microstructure`

- $l_0, l_1 \leftarrow$ sample indices of phases 0 and 1 with different-phase neighbors `// use Eq. (12)`
- $\hat{\mathbf{M}}^{\text{prev}} \leftarrow \hat{\mathbf{M}}^{\text{rec}}$ `// store variables`
- $\hat{\mathbf{M}}^{\text{rec}} \leftarrow$ mutation of $\hat{\mathbf{M}}^{\text{rec}}$ with values at locations l_0 and l_1 swapped
- **if** $\mathcal{L}(\hat{\mathbf{M}}^{\text{prev}}) < \mathcal{L}(\hat{\mathbf{M}}^{\text{rec}})$ **then** `// check if solution worsened, use Eq. (8) as loss`
  - $\hat{\mathbf{M}}^{\text{rec}} \leftarrow \hat{\mathbf{M}}^{\text{prev}}$ `// undo mutation`
- **end**
- $n_{\text{iter}} \leftarrow n_{\text{iter}} + 1$ `// increment counter`

end

Output: Post-processed microstructure $\hat{\mathbf{M}}^{\text{rec}}$

The procedure is effectively a version of the Yeong-Torquato algorithm [62] with an acceptance criterion as in the Great Deluge [12] and a type of different-phase-neighbor (DPN) sampling rule [67, 45]. Indeed, the procedure is practically implemented as an optimizer plugin that is added to *MCRpy* upon acceptance of this work. The difference to a full-fledged reconstruction algorithm is that we can expect to be close to the solution and only want to minimize noise. This motivates the zero-tolerance pixel swap criterion and also allows for the number of iterations as low as $\mathcal{O}(10^4)$, as opposed to up to $\mathcal{O}(10^9)$ as in the Yeong-Torquato algorithm [1].

The settings used in this work are identical to the reconstruction settings in Table 1 except that multigrid reconstruction is not applicable and 20,000 iterations are used. In this context, it is worth noting that in each iteration, the descriptors only need to be computed on slices that are affected by pixel swaps. Therefore, although more iterations are used for post-processing than for the actual reconstruction, the computational cost per iteration is much lower.

2.4. Numerical Simulation and Homogenization

The numerical simulations are conducted in *DAMASK* [49], which comprises efficient FFT-based solvers for regular grids. This enables the simulations directly on voxel data, which is readily available as the reconstruction output,

without introducing discretization errors that would arise from approximating the reconstruction output by, e.g. a tetrahedral mesh.

2.4.1. Constitutive Model

The assumed elasto-plastic constitutive behavior of the individual phases within the simulations is described in the following. A more detailed description of this model is given in [49]. Therein, DAMASK, a toolbox mainly designed for crystal plasticity simulations, is presented. Despite the advanced capabilities of DAMASK, the present work uses it merely in a reduced form with a fully phenomenological plasticity model without considering individual grains.

As usual in finite strain inelasticity, the multiplicative decomposition[4] $\boldsymbol{F} = \boldsymbol{F}^{\mathrm{e}} \cdot \boldsymbol{F}^{\mathrm{p}}$ of the deformation gradient $\boldsymbol{F}$ into elastic $\boldsymbol{F}^{\mathrm{e}}$ and plastic $\boldsymbol{F}^{\mathrm{p}}$ parts is assumed, where $\boldsymbol{F}^{\mathrm{p}}$ is purely isochoric. Thus, the elastic Green-Lagrange strain tensor $\boldsymbol{E}^{\mathrm{e}}$ is given by $\boldsymbol{E}^{\mathrm{e}} := \frac{1}{2}\left[(\boldsymbol{F}^{\mathrm{e}})^T \cdot \boldsymbol{F}^{\mathrm{e}} - \boldsymbol{I}\right]$, where $\boldsymbol{I}$ denotes the unit tensor. Assuming a Saint Venant-Kirchhoff model for the stress-strain relation, the second Piola-Kirchhoff stress tensor $\boldsymbol{S}$ is linked to $\boldsymbol{E}^{\mathrm{e}}$ by

$$\boldsymbol{S} = \mathbb{C} : \boldsymbol{E}^{\mathrm{e}} \,, \tag{13}$$

where $\mathbb{C}$ denotes the fourth-order stiffness tensor.

Plasticity is approached in a regularized manner by a rate-dependent model. The evolution of the plastic deformation gradient is given in terms of the plastic velocity gradient

$$\boldsymbol{L}^{\mathrm{p}} = \frac{\dot{\gamma}_{\mathrm{p}}}{3} \frac{\boldsymbol{S}^{\mathrm{dev}}}{\|\boldsymbol{S}^{\mathrm{dev}}\|_{\mathrm{F}}} \,. \tag{14}$$

by the flow rule $\dot{\boldsymbol{F}}^{p} = \boldsymbol{L}^{\mathrm{p}} \cdot \boldsymbol{F}^{\mathrm{p}}$. For the case of isotropic plasticity and purely isochoric plastic deformation, the plastic strain rate $\dot{\gamma}_{\mathrm{p}}$ is modeled by the phenomenological power law

$$\dot{\gamma}_{\mathrm{p}} = \dot{\gamma}_0 \left(\sqrt{\frac{3}{2}} \frac{\|\boldsymbol{S}^{\mathrm{dev}}\|_{\mathrm{F}}}{M\xi} \right)^{n} \,, \tag{15}$$

where $M = 3$ and $\dot{\gamma}_{\mathrm{p}}$ depends on the initial strain rate $\dot{\gamma}_0$, the stress exponent n, the Frobenius norm $\|(\bullet)\|_{\mathrm{F}}$ of the deviatoric part $\boldsymbol{S}^{\mathrm{dev}} := \boldsymbol{S} - \frac{1}{3}\boldsymbol{I}\,\mathrm{tr}(\boldsymbol{S})$ of the second Piola-Kirchhoff stress and the material resistance ξ. Herein,the evolution of ξ from its initial value ξ_0 towards its final value ξ_∞ is given by

$$\dot{\xi} = \dot{\gamma} h_0 \left| 1 - \frac{\xi}{\xi_\infty} \right|^{a} \mathrm{sign}\left(1 - \frac{\xi}{\xi_\infty} \right) \,, \tag{16}$$

where h_0 denotes the initial hardening and a is a fitting parameter. The numerical values of the material properties of each phase are summarized in Table 2 in Section 3.

2.4.2. Numerical Homogenization

To determine the effective elastic and plastic properties of the considered heterogeneous materials, a *computational homogenization* framework is applied. Following common practice, the effective deformation gradient $\bar{\boldsymbol{F}}$ and first Piola-Kirchhoff stress tensor $\bar{\boldsymbol{P}}$ are defined by

$$\bar{\boldsymbol{F}} := \langle \boldsymbol{F} \rangle \quad \text{and} \quad \bar{\boldsymbol{P}} := \langle \boldsymbol{P} \rangle \,, \tag{17}$$

where $\langle(\bullet)\rangle$ is the volume averaging operator and $\bar{(\bullet)}$ labels effective quantities in the following. Other effective quantities such as the Green-Lagrange strain $\bar{\boldsymbol{E}} := \frac{1}{2}\left[\bar{\boldsymbol{F}}^T \cdot \bar{\boldsymbol{F}} - \boldsymbol{I}\right]$ and $\bar{\boldsymbol{S}}$ cannot be obtained directly by averaging the local fields, but need to be computed from $\bar{\boldsymbol{F}}$ and $\bar{\boldsymbol{P}}$. To fulfill the Hill-Mandel condition, periodic boundary conditions are applied.

[4] Within the original model [49], the split $\boldsymbol{F} = \boldsymbol{F}^{\mathrm{e}} \cdot \boldsymbol{F}^{\mathrm{i}} \cdot \boldsymbol{F}^{\mathrm{p}}$ into elastic, lattice-distorting inelastic and lattice-preserving inelastic parts is applied. Here, $\boldsymbol{F}^{\mathrm{i}}$ is set to $\boldsymbol{I}$. Due to this, Mandel stress in the plastic configuration $\boldsymbol{M}^{\mathrm{p}} = (\boldsymbol{F}^{\mathrm{i}})^T \cdot \boldsymbol{F}^{\mathrm{i}} \cdot \boldsymbol{S}$ and second Piola-Kirchhoff stress coincide.

The effective elastic properties of the material, i.e., the case that $\boldsymbol{F}^{\mathrm{p}} = \boldsymbol{I}$, are given by means of the full stiffness tensor $\bar{\mathbb{C}}$. As a simple way to determine $\bar{\mathbb{C}}$, six load cases are chosen such that only one or two entries of $\bar{\boldsymbol{E}}$ are non-zero. This is achieved by prescribing

$$[\bar{E}_{kl}] = \frac{1}{2}\begin{bmatrix} \bar{\lambda}^2 - 1 & 0 & 0 \\ 0 & 0 & 0 \\ 0 & 0 & 0 \end{bmatrix}, \quad \text{i.e.,} \quad [\bar{F}_{kl}] = \begin{bmatrix} \bar{\lambda} & 0 & 0 \\ 0 & 1 & 0 \\ 0 & 0 & 1 \end{bmatrix}, \tag{18}$$

for tension and

$$[\bar{E}_{kl}] = \frac{1}{2}\begin{bmatrix} 0 & \bar{\gamma}/2 & 0 \\ \bar{\gamma}/2 & 0 & 0 \\ 0 & 0 & 0 \end{bmatrix}, \quad \text{i.e.,} \quad [\bar{F}_{kl}] = \begin{bmatrix} \bar{\gamma}/(2\delta) & \delta & 0 \\ \delta & \bar{\gamma}/(2\delta) & 0 \\ 0 & 0 & 1 \end{bmatrix}, \tag{19}$$

for shear, where

$$\delta = \sqrt{\frac{1}{2}\left(1 - \sqrt{1 - \bar{\gamma}^2}\right)}. \tag{20}$$

Herein, $\bar{\gamma}$ denotes the shear and $\bar{\lambda}$ is the stretch. Analogous load cases are chosen for tension and shear in the other two directions. It follows that

$$\bar{C}_{ij11} = \frac{\bar{T}^{11}_{ij}}{\bar{E}^{11}_{11}} \qquad \bar{C}_{ij22} = \frac{\bar{T}^{22}_{ij}}{\bar{E}^{22}_{22}} \qquad \bar{C}_{ij33} = \frac{\bar{T}^{33}_{ij}}{\bar{E}^{33}_{33}} \tag{21}$$

and

$$\bar{C}_{ij23} = \frac{\bar{T}^{23}_{ij}}{2\bar{E}^{23}_{23}} \qquad \bar{C}_{ij13} = \frac{\bar{T}^{13}_{ij}}{2\bar{E}^{13}_{13}} \qquad \bar{C}_{ij12} = \frac{\bar{T}^{12}_{ij}}{2\bar{E}^{12}_{12}}\,, \tag{22}$$

where the subscript denotes the tensor component and the superscript denotes the load case.

Furthermore, in order to characterize the effective plastic properties of the considered materials, stress-deformation states, e.g.,

$$[\bar{F}_{kl}] = \begin{bmatrix} \bar{F}_{11} & 0 & 0 \\ 0 & - & 0 \\ 0 & 0 & - \end{bmatrix} \tag{23}$$

are prescribed within the computational homogenization. Analogous states are applied into the x_2- and x_3-directions.

2.4.3. Visualization of Effective Stiffness

Instead of numerically listing all components of $\bar{\mathbb{C}}$, elastic surface plots are used for visualization [8, 44]. As shown in Figure 2 for isotropic, transversally isotropic and cubic material behavior, for each orientation (φ, θ) in a spherical coordinate system[5], the radius of the elastic surface is given by the directional Young's modulus $\bar{E}(\varphi, \theta)$ that would be measured under tension in this orientation. Using the effective stiffness tensor in Voigt notation $\bar{\mathbf{C}}^{\mathrm{V}}$, it can be extracted from the transformed compliance matrix

$$\bar{\mathbf{N}}' = \left(\mathbf{Q} \cdot \bar{\mathbf{C}}^{\mathrm{V}} \cdot \mathbf{Q}^{\mathrm{T}}\right)^{-1} \tag{24}$$

as

$$\bar{E}(\varphi, \theta) = \frac{1}{\bar{N}'_{11}} \quad , \tag{25}$$

[5]Herein, $\varphi \in [0,\ 2\pi]$ quantifies the azimuthal angle, i.e., the rotation around the **z**-axis, whereas $\theta \in [0,\ \pi]$ is the polar angle.

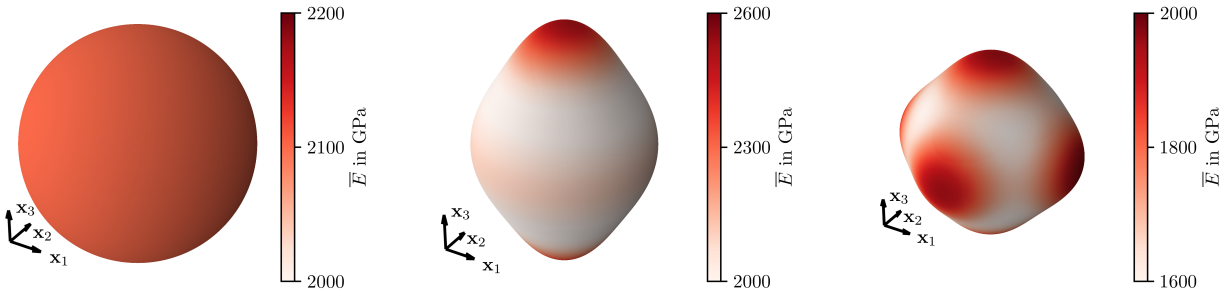

(a) Isotropic (b) Transversally isotropic (c) Cubic

Figure 2: Exemplary elastic surface plots for an isotropic (a), a transversally isotropic (b) and a cubic (c) material model.

where

$$[\mathbf{Q}]_{kl} = \begin{bmatrix} b_{11}b_{11} & b_{12}b_{12} & b_{13}b_{13} & 2b_{12}b_{13} & 2b_{11}b_{13} & 2b_{11}b_{12} \\ b_{21}b_{21} & b_{22}b_{22} & b_{23}b_{23} & 2b_{22}b_{23} & 2b_{21}b_{23} & 2b_{21}b_{22} \\ b_{31}b_{31} & b_{32}b_{32} & b_{33}b_{33} & 2b_{32}b_{33} & 2b_{31}b_{33} & 2b_{31}b_{32} \\ b_{21}b_{31} & b_{22}b_{32} & b_{23}b_{33} & b_{22}b_{33}+b_{32}b_{23} & b_{21}b_{33}+b_{31}b_{23} & b_{21}b_{32}+b_{31}b_{22} \\ b_{11}b_{31} & b_{12}b_{32} & b_{13}b_{33} & b_{12}b_{33}+b_{32}b_{13} & b_{11}b_{33}+b_{31}b_{13} & b_{11}b_{32}+b_{31}b_{12} \\ b_{11}b_{21} & b_{12}b_{22} & b_{13}b_{23} & b_{12}b_{23}+b_{22}b_{13} & b_{11}b_{23}+b_{21}b_{13} & b_{11}b_{22}+b_{21}b_{12} \end{bmatrix} \tag{26}$$

with

$$[\mathbf{b}]_{kl} = \begin{bmatrix} \sin\theta\cos\varphi & \sin\theta\sin\varphi & \cos\theta \\ \cos\theta\cos\varphi & \cos\theta\sin\varphi & -\sin\theta \\ -\sin\varphi & \cos\varphi & 0 \end{bmatrix} \quad . \tag{27}$$

2.4.4. Plastic Properties

The effective plastic properties investigated in this work are limited to the computation of the effective yield strength in three directions, since the determination of the full yield surface would exceed the scope of this work. For this purpose, uniaxial tension according to Eq. (23) is applied and the yield strength $\bar{\sigma}_y$ is defined by a plastic strain of $\bar{E}^p = 0.2\%$, where $\bar{E}^p$ is obtained from $\bar{E}$ by subtracting the elastic part.

3. Data for Validation

Motivated by the advent of additive manufacturing and metamaterials and the complex resulting structure-property linkages, a novel titanium alloy and a "bone-like" spinodoid structure are considered in Sections 3.1 and 3.2, respectively.

3.1. Titanium Alloy on Microscale

On the microscale, a new alloy developed for laser powder bed fusion is used as a representative microstructure. The alloy and experimental methods are described in detail in [21] and a brief summary is given in the following. The titanium-rich binary eutectic material (Ti-32.5Fe, wt.%) was produced by in-situ alloying using elemental powder blends during high temperature laser powder bed fusion at a temperature of $\theta \approx 600$ °C in an SLM Solutions 280 HL machine. The near-field ptychographic X-ray tomography experiments were performed with micrometer-sized cylinders (diameter $d = 18$ µm and height $h = 40$ µm, extracted from the material by focused ion beam milling) at the ID16A nano-imaging beamline of the European Synchrotron Radiation Facility (ESRF) [14]. The processing of the tomographic volume of each sample was carried out in three steps: *(i)* phase retrieval of the near-field ptychographic imaging scan at each tomographic angle, *(ii)* pre-processing of the retrieved tomographic projections and *(iii)* tomographic reconstruction. The segmentation of the two major microstructural constituents (hereafter called β-Ti

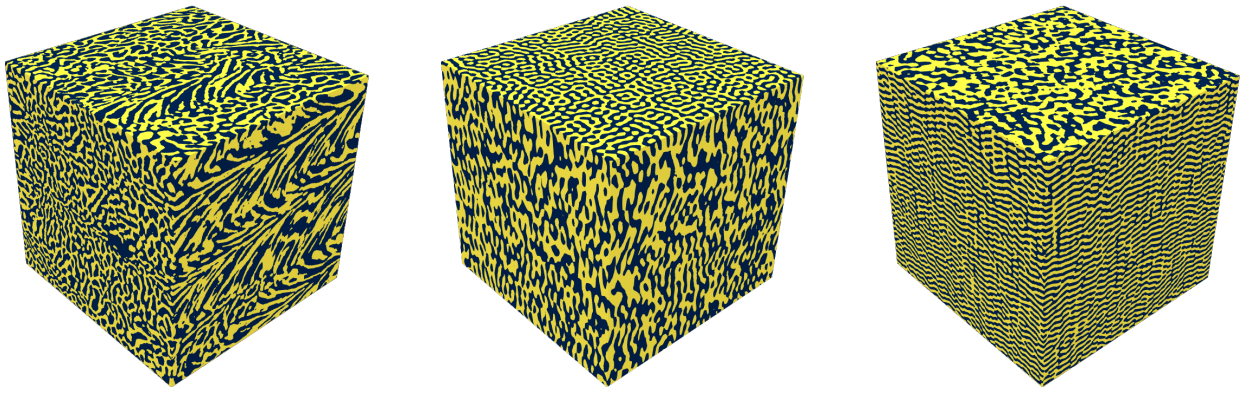

(a) Real Ti-Fe scan [21] (10 µm) (b) Synthetic columnar structure (10 cm) (c) Synthetic lamellar structure (10 cm)

Figure 3: Original 3D structures used for the validation with the length of the samples given in parentheses. The Ti-Fe alloy (a) is a real CT scan in the microscale, whereas (b) and (c) are synthetically generated mesoscale structures.

Table 2
Material parameters for the micro- and mesoscale simulations.

Parameter	Microscale		Mesoscale	
	β-Ti	TiFe	Ti alloy	Void
$\mathbb{C}_{1111}$ in GPa	174.6	298.0	218.3	0.2
$\mathbb{C}_{1122}$ in GPa	82.2	135.8	97.9	0.0
$\mathbb{C}_{1123}$ in GPa	46.2	81.1	60.2	0.1
ξ_0 in MPa	535.1	572.0	530	-
ξ_∞ in MPa	1426.0	1525.6	1400.0	-
h_0 in MPa	713.3	762	700	-
$\dot{\gamma}_0$	0.001	0.001	0.001	-
n	20	20	20	-
a	2	2	2	-

and TiFe) was carried out after pre-processing the reconstructed volumes using bandpass filters available in Fiji [53] and Avizo Fire 9.5 to enhance their quality. As a reference structure for the present work, a statistically homogeneous cuboid of length $l = 10$ µm is extracted from the CT scan and shown in Figure 3.

The material parameters of the individual phases for the numerical simulations are taken from the literature [52, 69, 70] and are summarized in Table 2.

3.2. Spinodoid Structure on Mesoscale

On the mesoscale, "bone-like" spinodoid structures are reconstructed and homogenized using the effective material parameters from the microscale to demonstrate the ability to accurately capture highly anisotropic stiffness tensors. Spinodoid structures are very resilient due to the absence of notches [25] and have received much attention lately in inverse design of anisotropic stiffness [33] in combination with topology optimization [68]. Potential applications are the design of synthetic bones with tunable stiffness or the general design of resilient metamaterials.

In the absence of data, the reference structures do not stem from a CT scan, but are generated from *GIBBON* [41]. Based on the work of Kumar et al. [33], *GIBBON* allows to generate spinodoid structures from a low-dimensional parametrization using Gaussian random fields. For the validation of the reconstruction, we use this parametrization to generate two reference structures and pretend they might stem, e.g., from a bone [33]. As shown in Figure 3, a columnar and a lamellar structure are considered in this work, both with a volume fraction of 50 %.

The properties of the bulk material are taken from the homogenized response of the microscale domain, which is presented in Section 4. While the elastic properties can be obtained directly, the plastic properties ξ_0, ξ_∞ and h_0 are estimated from the effective yield strength by a rule of proportion. Due to the inability of the chosen numerical

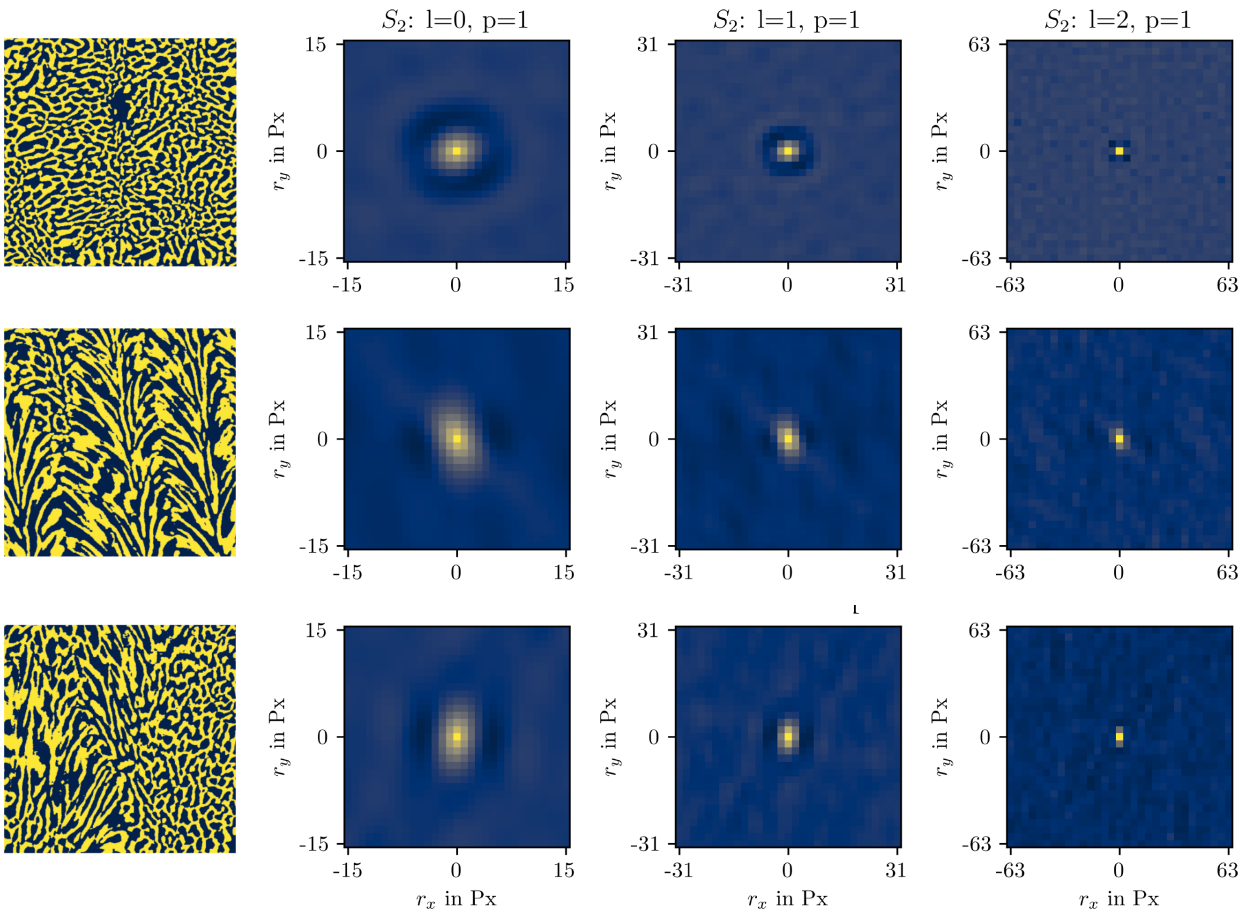

Figure 4: Schematic visualization of the computation of statistical descriptors from the three orthogonal sections extracted from the 3D reference in Figure 3. In this example, the spatial two-point autocorrelation of phase $p = 1$ is shown. These descriptors are used in this work and complemented by higher-order correlations, Gram matrices and the variation. From left to right, it can be seen that short-distance correlations are computed with the highest accuracy (multigrid level $l = 0$), whereas longer-range correlations are computed on down-sampled versions ($l = 1, 2$) of the structure as described in [56].

solver to represent voids, a purely elastic material model is chosen with a phase contrast of approximately 1000 in the stiffness. The parameters of both material models are summarized in Table 2.

4. Results and Discussion

Section 4.1 presents the result of the microstructure reconstruction. After a qualitative and quantitative analysis of the statistical descriptors of the reconstructed structure in Section 4.2, a validation of the effective properties is carried out for the microscale alloy and the mesoscale metamaterial in Sections 4.3 and 4.4, respectively.

4.1. Reconstruction results

For each of the original structures in Figure 3, three orthogonal slices are extracted, down-sampled[6] to 256×256 pixels and used for the computation of microstructure descriptors as shown schematically for the Ti-Fe structure in Figure 4. As described in Section 2.1, the spatial three-point correlations, the Gram matrices and the variation are used as microstructure descriptors.

[6]This is done to allow for the reconstructed microstructures to "only" have a resolution of 128^3 voxels and still be large enough to adequately represent the morphology. Although resolutions of up to 512^3 voxels have already been reconstructed with *MCRpy* [57], this currently requires amounts of computational resources that we find impractical for the large number of structures considered in this work.

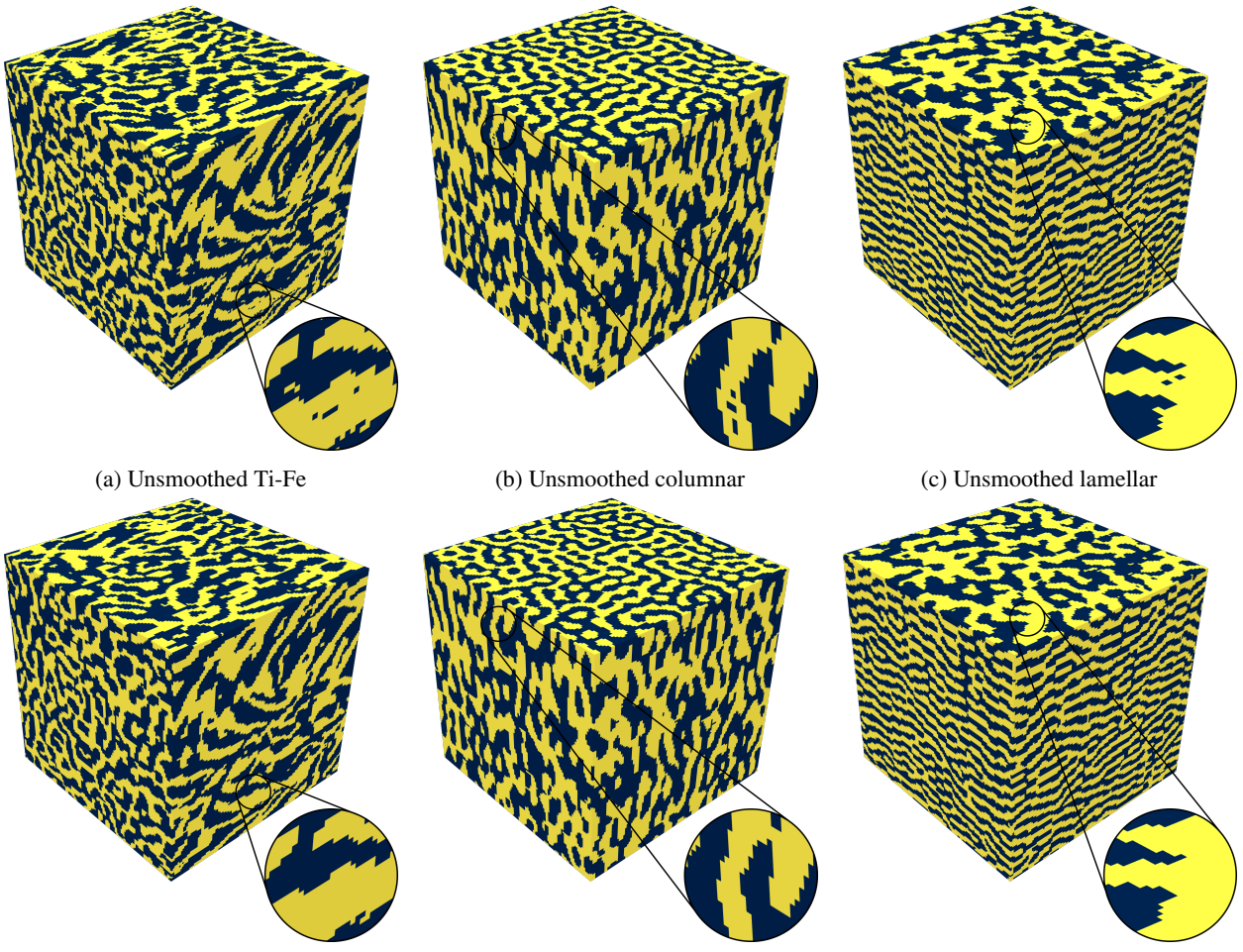

(a) Unsmoothed Ti-Fe (b) Unsmoothed columnar (c) Unsmoothed lamellar

(d) Smoothed Ti-Fe (e) Smoothed columnar (f) Smoothed lamellar

Figure 5: The effect of descriptor-based smoothing on the reconstructed structures: It can be seen that spurious noise is eliminated while sharp microstructural features are preserved.

MCRpy is used for the reconstruction as described in Section 2.2 as well as for the smoothing procedure outlined in Section 2.3. With a resolution of 128^3 voxels, the former took 7 hours for 800 iterations[7] on a single *Nvidia A100* GPU, whereas the latter required 3 hours for $20,000$ iterations on the same hardware. The effect of the smoothing is illustrated in Figure 5. Although for the present microstructures the authors found that simpler and more efficient smoothing procedures based on Gaussian filtering also work (not shown here), this is not always the case as discussed in Appendix A. Per structure, 20 instances are created to compare the variation between random realizations[8] to the deviation from the reference structure.

After the reconstruction and subsequent smoothing, the generated structures are visually very similar to the references as shown in Figure 6. To support this qualitative statement, a quantitative morphology analysis is carried out based on spatial correlations. First, the statistical distribution of 2D correlations over all slices is analyzed for the original and reconstructed structure. Then, the fully 3D two-point correlations are directly compared.

[7] More precisely, 800 iterations are performed per multigrid level. The three multigrid levels took 20 minutes, 1.5 hours and 5 hours respectively. The last multigrid level on the highest resolution could have been aborted after 400 iterations with a very similar outcome, leading to a total wall-clock time of 4.5 hours, but this was not done.

[8] As mentioned in [57], the solution found by the optimizer in 3D reconstruction depends on the initial value. Hence, a different random seed can be used to generate different, but statistically equivalent structures, herein called realizations.

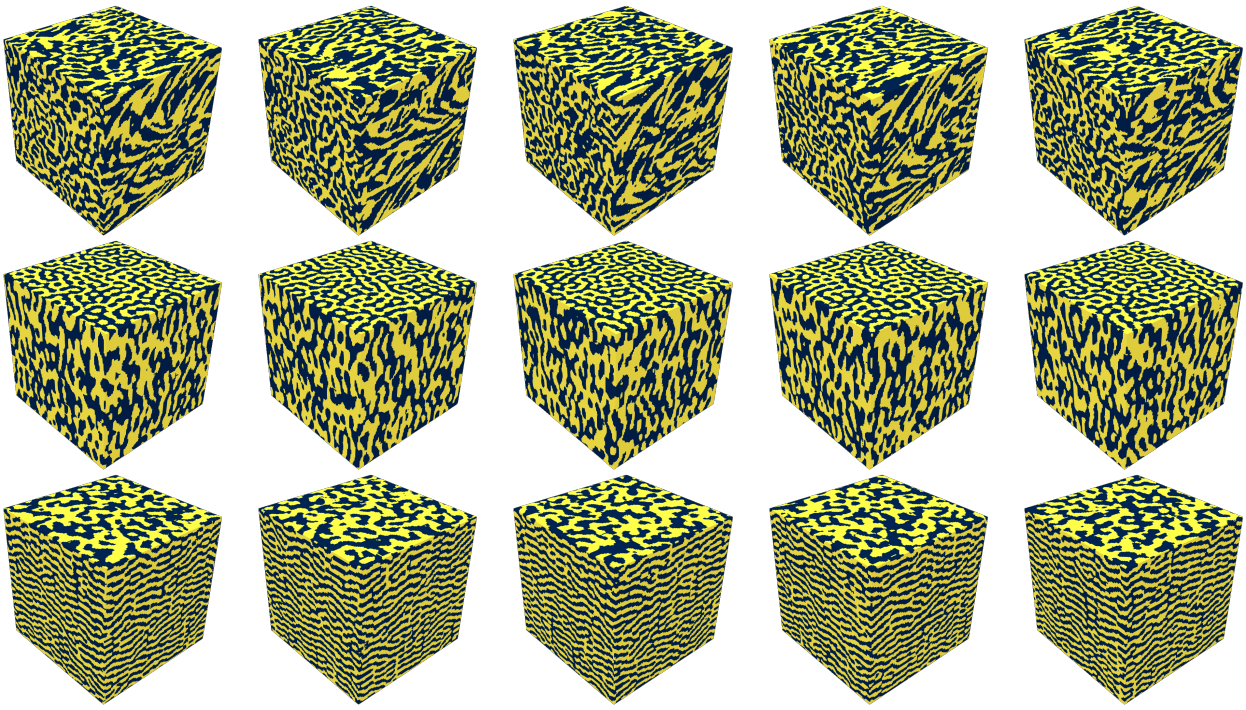

Figure 6: Five reconstruction examples per structure for the real Ti-Fe material (top) and the columnar (center) and lamellar (bottom) synthetic structure.

4.2. Descriptor errors

In order to visually analyze the high-dimensional two-point correlations, a principal component analysis (PCA) is used to reduce them to two dimensions. In Figure 7, the original microstructure is exemplarily compared to the first reconstructed structure shown in Figure 6 in terms of the first two modes of the slice descriptors. It is worth noting that the 2D-to-3D reconstruction is not informed about the entire distribution of original descriptors, which would describe the entire 3D structure, but only one randomly chosen value which corresponds to the single original 2D slice. Based on this discrepancy, three phenomena are discussed based on simple volume fractions and are identified in Figure 7 for spatial correlations:

(i) *Descriptor concentration*: Due to random variations in the microstructure, the volume fraction of a single slice might be higher or lower than that of the entire microstructure. The expected magnitude of these fluctuations decreases as the microstructure size increases. Since the reconstruction is not based on the statistical distribution of volume fractions, but on a single value, there is no control of the fluctuations. Analogously, for generic descriptors, the descriptors in the reconstructed slices is observed to scatter less than in the original structure in Figure 7.

(ii) *Descriptor difference*: Due the same variations in the microstructure, the prescribed value of the volume fraction is not optimal. A similar phenomenon can be observed for generic descriptors. In Figure 7 (a), the prescribed descriptor is close to the boundary of the original descriptor point cloud. Therefore, although the descriptors of the reconstructed structure are centered around the prescribed value, a discrepancy is observed.

(iii) *Descriptor incompatibility*: Moreover, the random fluctuations of the slice descriptors can lead to contradictions between orthogonal slices. For example, it is impossible to achieve a volume fraction of $v_\mathrm{f} = 5\%$ on all slices in x_1-direction while at the same time requiring $v_\mathrm{f} = 6\%$ on all slices in x_2-direction. The average of the loss function over all slices and dimensions in Eq. (9) leads to a compromise between incompatible descriptors, which manifests itself as offset between the mean descriptor of the reconstructed slices and the prescribed value. For generic descriptors, this phenomenon can be observed in Figures 7 (b) and (c).

Because the purpose of Figure 7 is a discussion of qualitative trends, only a single reconstructed structure is shown. Similar trends can be observed for all reconstructed structures. While the principal components are well-suited for

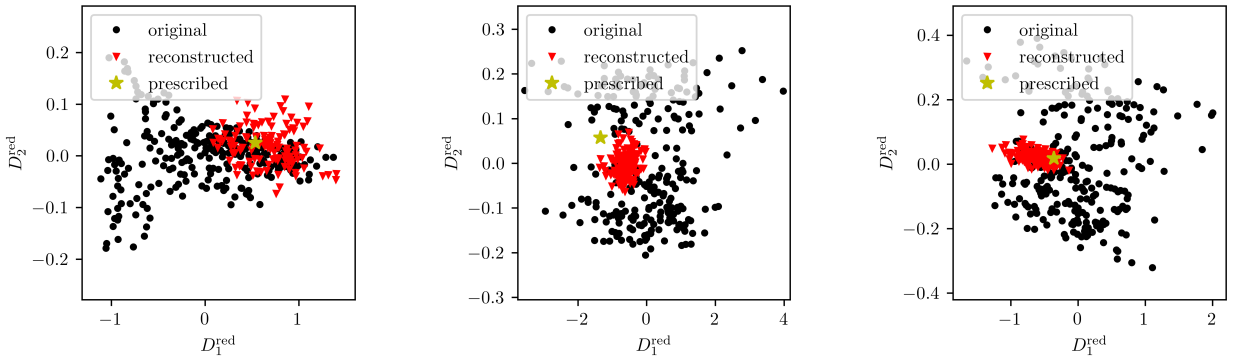

(a) Slicing in x_1-direction (b) Slicing in x_2-direction (c) Slicing in x_3-direction

Figure 7: Low-dimensional analysis of the descriptor distribution over the slices of the original and reconstructed Ti-Fe structure. Herein, every marker denotes a descriptor value, which is either prescribed during optimization or computed on a single slice of the original or reconstructed structure.

Table 3
Errors of the full 3D two-point correlations.

	$\max_\alpha \mathcal{E}_D^{\text{abs}}(\mathbf{M}_\alpha^{\text{rec}})$	$\frac{1}{20}\sum_\alpha \mathcal{E}_D^{\text{abs}}(\mathbf{M}_\alpha^{\text{rec}})$	$\max_\alpha \mathcal{E}_D^{\text{rel}}(\mathbf{M}_\alpha^{\text{rec}})$	$\frac{1}{20}\sum_\alpha \mathcal{E}_D^{\text{rel}}(\mathbf{M}_\alpha^{\text{rec}})$
Alloy	$3.01 \cdot 10^{-5}$	$2.84 \cdot 10^{-5}$	0.071%	0.067%
Columnar	$2.66 \cdot 10^{-5}$	$2.52 \cdot 10^{-5}$	0.043%	0.040%
Lamellar	$2.94 \cdot 10^{-5}$	$2.88 \cdot 10^{-5}$	0.046%	0.045%

discussing qualitative trends in point clouds, the magnitude of the errors can not be assessed very well. The absolute and relative descriptor error between original (og) and reconstructed (rec) structure are measured given by

$$\mathcal{E}_D^{\text{abs}} = ||\mathbf{S}_2^{3\text{D}}(\mathbf{M}^{\text{rec}}) - \mathbf{S}_2^{3\text{D}}(\mathbf{M}^{\text{og}})||_{\text{MSE}} \tag{28}$$

and

$$\mathcal{E}_D^{\text{rel}} = \mathcal{E}^{\text{abs}} / ||\mathbf{S}_2^{3\text{D}}(\mathbf{M}^{\text{og}})||_{\text{MSE}}. \tag{29}$$

Note that this comprises the full 3D correlations computed with the software *pyMKS* [6] and not a slice-wise comparison. The maximum and average error of all 20 reconstructed microstructures is given in Table 3. With less than 0.1% deviation, the 3D two-point correlation is captured very well. However, it presently not clear how small a descriptor error should be in order to guarantee similar effective properties. Therefore, the homogenized material response is analyzed in the following.

4.3. Effective alloy properties

The effective properties of the titanium alloy are quantified in terms of the elastic and plastic behavior.

The elastic behavior is captured by the full stiffness tensor, which is visualized by means of *elastic surface* or *YMS* plots [8, 44], see Section 2.4. A comparison between the simulations based on the original CT scan and the first reconstructed structure is given in Figure 8. Table 4 enables a quantitative comparison of $\bar{E}$ in x_1-, x_2- and x_3-direction. It can be seen that the range of the Young's modulus as well as the degree of anisotropy is captured very well. The exact direction of the anisotropy slightly differs from the correct value. However in Table 4, for each reconstructed structure, the effective Young's modulus in a certain direction is closer to the reference modulus in the same direction than to the reference modulus in another direction. Overall, the relative error

$$\mathcal{E}_E^{\text{rel}} = \frac{\bar{E}^{\text{rec}} - \bar{E}^{\text{og}}}{\bar{E}^{\text{og}}} \tag{30}$$

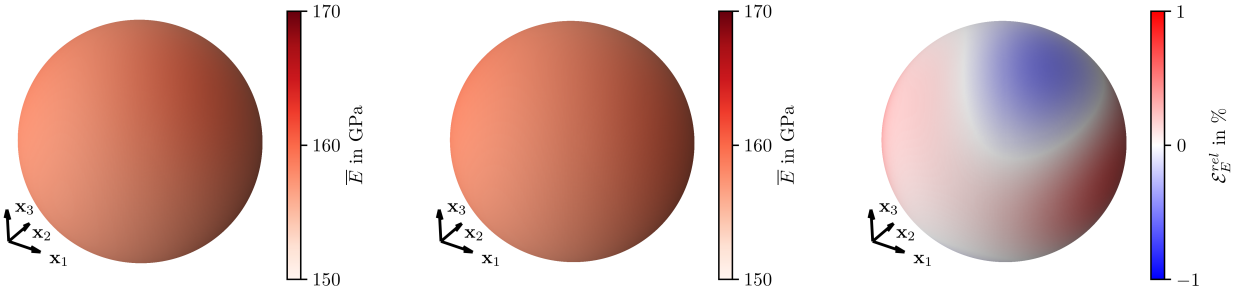

(a) Original structure (b) Reconstructed structure (c) Difference

Figure 8: Elastic surface plots of the original and generated Ti-Fe structure.

Table 4
Errors of the effective directional Young's modulus and yield strength for the Ti-Fe structure.

Direction	$\bar{E}^{\text{ref}}$ in GPa	$\bar{E}^{\text{rec}}$ in GPa	$\mathcal{E}_{\text{E}}$ in %	$\bar{\sigma}_{\text{y}}^{\text{ref}}$ in MPa	$\bar{\sigma}_{\text{y}}^{\text{rec}}$ in MPa	$\mathcal{E}_{\sigma_{\text{y}}}$ in %
x	158.383	159.346 ± 0.006	0.61	1417.69	1400.53 ± 0.18	-1.21
y	156.713	156.864 ± 0.005	0.10	1455.76	1455.73 ± 0.23	-0.00
z	157.825	157.515 ± 0.006	-0.20	1428.05	1439.74 ± 0.21	0.82

of the directional Young's modulus is limited to approximately ±0.5% with a maximum error of 0.61%, which is extremely small considering a phase contrast of $E^{\text{TiFe}}/E^{\beta-\text{Ti}} \approx 2$. As a comparison, for the same material properties, simple homogenization by Voigt's and Reuss' formulae yield an upper and lower bound of 163.3 GPa and 151.3 GPa, respectively.

The plastic material response is quantified by the effective yield strength $\bar{\sigma}_{\text{y}}$, whereby this work is limited to the x_1-, x_2- and x_3-direction for computational efficiency. The results are summarized in Table 4. Again, all relative errors

$$\mathcal{E}_{\sigma_y}^{\text{rel}} = \frac{\bar{\sigma}_y^{\text{rec}} - \bar{\sigma}_y^{\text{og}}}{\bar{\sigma}_y^{\text{og}}} \tag{31}$$

are very small, and the anisotropy of the effective properties is captured very well.

Figure 9 shows the scatter of the effective isotropic elasto-plastic properties compared to the reference. Note that the reference is different for each spatial direction, as can be seen in Table 4. However, as shown in Table 3, the differences within the reconstructed structures are much smaller than the deviation between the reconstructed and original structure. This is likely attributable to the systematic descriptor deviations mentioned in Section 4.2 and is discussed further in the following section with a higher degree of anisotropy.

Finally, Figure 10 shows the material response of the original structure and the first reconstruction result under two load cycles. Also in this case, it can be seen that the effective behavior is captured very well and even at a large magnification, the difference between the curves is very small. The response under load in the other directions is predicted similarly well.

4.4. Properties of spinodoid metamaterial

Based on the effective properties to the Ti-Fe system identified in the previous section, the elasto-plastic material model introduced in Subsec. 2.4.1 is parametrized as given in Table 2. It is used to determine the macroscopic properties of the spinodoid, "bone-like" materials. This poses several challenges because with increasing phase contrast and anisotropy, (i) both, original as well as reconstructed structures, need to be increasingly large to adequately capture the morphology, (ii) small errors in reconstructing highly stressed parts of the structure can lead to spurious local stress concentrations and hence strongly affect the effective behavior, and (iii) for the same reason, noise that is inherent to 2D-to-3D reconstruction [4, 57] becomes increasingly problematic. The remainder of this section shows the results, which are surprisingly accurate considering the above challenges. Further investigations on the effect of insufficiently large volume elements and the effect of smoothing on the properties are given in Appendices B and C, respectively.

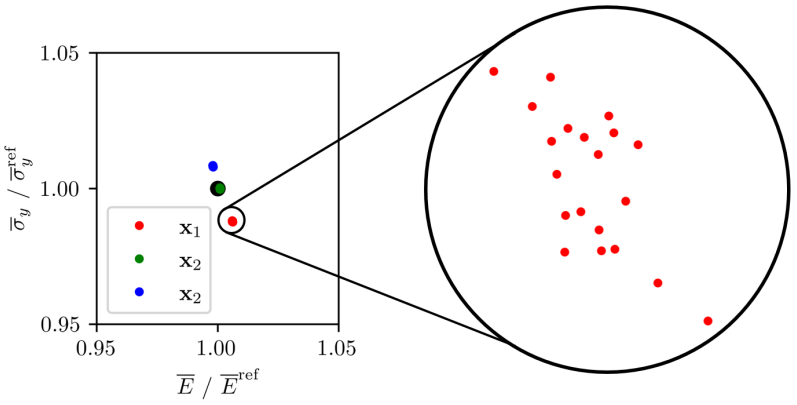

Figure 9: Relative error of the effective directional Young's modulus and yield strength for the Ti-Fe structures. It can be seen that the scatter over different realizations is much smaller than the systematic error. Note that all values are divided by the reference, but the reference is different in each direction. The numerical values are given in Table 4.

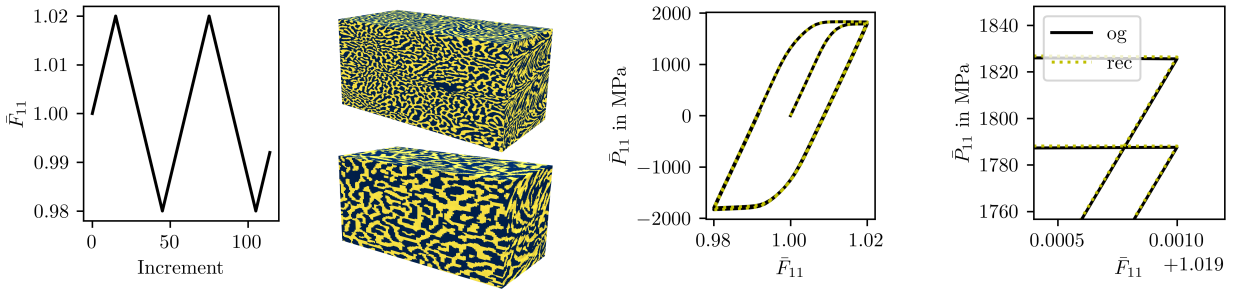

(a) Applied load case

(b) Displacement with magnification of 30

(c) Material response

(d) Zoom into (c)

Figure 10: Material response after two load cycles. The original structure (top, black) is compared to the first reconstruction result (bottom, yellow), illustrating the same qualitative and quantitative behavior.

The elastic surfaces of the original structure in Figure 3 and one reconstruction result (first column of Figure 6) are compared in Figure 11. As opposed to the Ti-Fe system in Figure 8, the elastic response of the spinodoid materials is highly anisotropic, making the result extremely sensitive to small errors in the reconstruction process. Nevertheless, the "rod-like" and "disc-like" shape of the elastic surfaces as well as their maximum radius are captured very well. The largest errors do no occur in the stiffest direction, but at an angle close to the stiffest direction. The reason for these errors is visualized by means of cuts through the elastic surfaces in Figure 12: Due to the very steep gradient of the elastic surfaces with respect to the load orientation, even small deviations in the orientation lead to large errors in the effective stiffness. The same applies to a slightly "thinner rod" in the columnar case or a slightly "flatter disk" in the lamellar case.

A quantitative comparison of the effective Young's modulus and yield stress is given in Table 5 and Figure 13. It can be seen that in x_1-, x_2- and x_3-direction, $\mathcal{E}_E$ stays within $\pm 5\%$ and the anisotropy is captured very well. As a comparison, for the same material properties, simple homogenization by Voigt's and Reuss' formulae yield an upper and lower bound of 80 GPa and 0.4 GPa[9], respectively, irrespective of loading direction.

In summary, the extreme phase contrast and strong anisotropy of the "bone-like" spinodoid structures naturally lead to larger errors compared to the real CT scan of the Ti-Fe system. Despite being synthetically constructed, the columnar and lamellar structure thus demonstrate the robustness of the reconstruction procedure.

[9]It should be mentioned that this lower bound is a purely numerical value, since the Fourier-based solver used in this work requires a non-zero stiffness to be assigned to the void phase as shown in Table 2. The correct lower bound by Reuss' formula is of course 0 GPa.

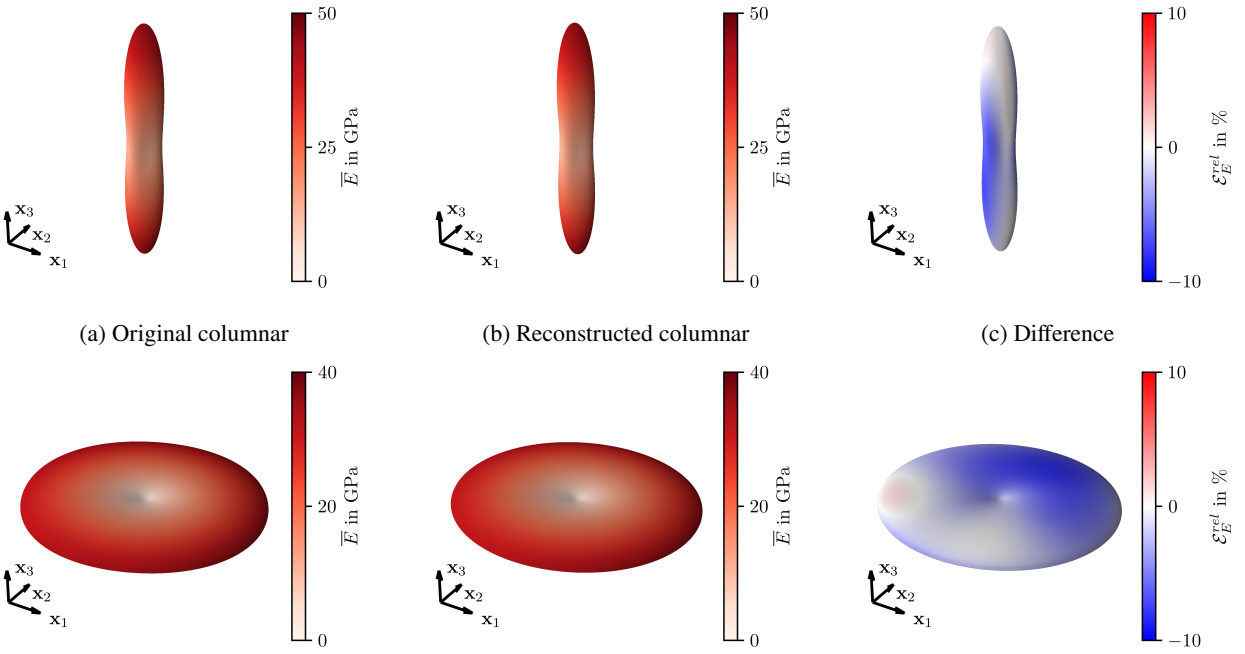

(a) Original columnar (b) Reconstructed columnar (c) Difference

(d) Original lamellar (e) Reconstructed lamellar (f) Difference

Figure 11: Elastic surface plots of the original and reconstructed spinodoid structures.

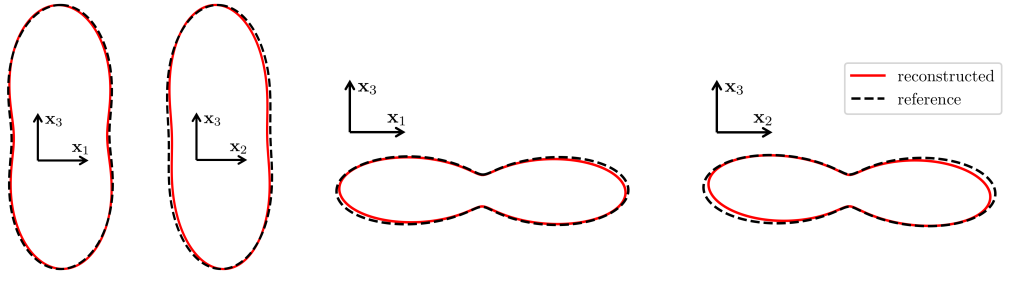

(a) Columnar, $\varphi = 0$ (b) Columnar, $\varphi = \pi/2$ (c) Lamellar, $\varphi = 0$ (d) Lamellar, $\varphi = \pi/2$

Figure 12: Cuts through Figure 11 (c) and (f) at $\varphi = 0$ and $\varphi = \pi/2$ reveal that a slightly wrong orientation of the elastic surface leads to large deviations in the radial direction.

5. Conclusions and Outlook

In this work, a two-stage optimization procedure is proposed to reconstruct 3D microstructures from 2D slices based on statistical descriptors.

As a *first* step, the recently developed differentiable microstructure characterization and reconstruction (DMCR) framework [56, 58] is utilized to quickly obtain a solution that minimizes the sum of descriptor errors over all microstructure slices. While this approach converges quickly and scales favorably, two problems remain: The given volume fractions are not guaranteed to be fulfilled after the real-valued reconstruction result $\mathbf{M}^{\text{rec}} \in \mathcal{M}^{3D}$ is projected to the integer-valued $\hat{\mathbf{M}} \in \hat{\mathcal{M}}^{3D}$ by element-wise rounding. Furthermore, despite employing the variation descriptor for noise reduction as highlighted in [4, 57], the remaining amount of noise cannot be neglected, motivating a tailored post-processing procedure.

Table 5
Errors of the effective directional Young's modulus and yield strength for the spinodoid structures.

	Direction	$\bar{E}^{\text{ref}}$ in GPa	$\bar{E}^{\text{rec}}$ in GPa	$\mathcal{E}_{\text{E}}$ in %	$\bar{\sigma}_{\text{y}}^{\text{ref}}$ in MPa	$\bar{\sigma}_{\text{y}}^{\text{rec}}$ in MPa	$\mathcal{E}_{\sigma_{\text{y}}}$ in %
col.	x	15.53	15.3 ± 0.15	-1.7	111.8	122 ± 1.8	9.3
	y	15.56	15.6 ± 0.12	0.23	113.4	121 ± 1.7	6.9
	z	43.03	43.1 ± 0.14	0.27	331.8	337 ± 3.1	1.5
lam.	x	32.06	31.2 ± 0.12	-2.7	257.8	256 ± 1.4	-0.6
	y	32.05	30.8 ± 0.11	-4.0	259.0	255 ± 1.5	-1.6
	z	3.55	3.4 ± 0.02	-3.1	45.99	43.5 ± 0.4	-5.4

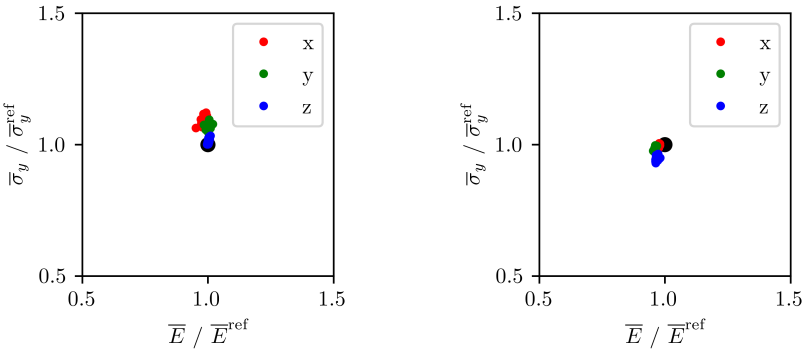

(a) Columnar structure

(b) Lamellar structure

Figure 13: Relative error of the effective directional Young's modulus and yield strength for the spinodoid structures. The zoom as in Figure 9 is omitted to avoid redundancy. Note that all values are divided by the reference, but the reference is different in each direction. The numerical values are given in Table 5.

As a *second* step, the microstructure is iteratively adjusted to the correct volume fractions and smoothed, whereby a custom algorithm distinguishes between sharp microstructural features and spurious noise by considering the previously computed microstructure descriptors. Starting from the Yeong-Torquato algorithm, a custom different-phase-neighbor sampling distribution and a zero-tolerance acceptance criterion are defined. These measures are implemented in order to account for the fact that the input data can be expected to already exhibit the desired morphology. Thus, the two-stage procedure makes use of the gradient-based optimization in DMCR while also employing microstructure descriptors to eliminate noise without degrading the microstructure quality.

A strong focus is placed on validating the 2D-to-3D reconstruction in terms of morphology and effective properties. For this purpose, a computed tomography (CT) scan of a recently developed β-Ti/TiFe alloy as well as morphologically extremely anisotropic "bone-like" spinodoid metamaterials are used as 3D reference structures. From each of these structures, three orthogonal slices are extracted to mimic the situation that only 2D information is available. Based on *only* these slices, statistical descriptors are computed and used for reconstructing 20 independent 3D realizations of each structure. The synthetic structures are visually very similar to their original counterpart and an in-depth quantitative analysis is carried out.

A detailed discussion of errors in the descriptor space classifies the sources of systematic deviations as descriptor *concentration*, *difference* and *incompatibility*. While the former is inherent to the formulation of the optimization problem and might be addressed in the future by formulating advanced cost functions, the latter two are expected to vanish as the structure for characterization becomes infinitely large. All phenomena are visualized by means of a scatter plot in the first two principal components of the descriptor space and the full 3D correlation errors are given for reference.

While there is no easy criterion to determine which magnitude of descriptor errors is acceptable, the effective properties are a practical indicator of whether the reconstructed structures match the reference. For this reason, elasto-plastic simulations are performed and a numerical homogenization is carried out in order to determine the full stiffness

tensor as well as the effective yield strength in three directions. The errors of the real Ti-Fe system are extremely small. For the synthetic spinodoid structures, the extreme anisotropy and high phase contrast naturally lead to higher deviations, however, a good prediction quality is reached and the anisotropy is captured very well.

In summary, the utility of the presented approach in reconstructing realistic 3D microscale domains from 2D slices is confirmed. This is an essential step towards making modern multiscale simulations more applicable to computational materials engineering. In this context, it is worth noting that all algorithms will be made freely available in the open-source software *MCRpy*. Thus, the excellent results in this study motivate further initiatives across disciplines in applying numerical multiscale simulations for computational materials engineering.

Declaration of competing interest

The authors declare no competing interest.

Acknowledgements

The authors thank Tobias Strohmann for his valuable input and for establishing the cooperation between the German Aerospace Center (DLR) and Technische Universität Dresden (TUD) on this subject. The authors appreciate the European Synchroton (ESRF), especially Da Silva and Cloetens at Beamline *ID16A* for their contributions. Furthermore, the authors thank Michał Basista and his colleagues at the Polish Academy of Sciences for providing data, which was unfortunately not suitable for this publication due to a volume fraction gradient. In this context, the authors also thank Ulrike Gebhardt at Technische Universität Dresden (TUD) for segmenting the same data. Finally, we thank Jörg Brummund (TUD) for the discussions and support regarding material modeling.

The group of M. Kästner thanks the German Research Foundation DFG which supported this work under Grant number KA 3309/18-1. The authors are grateful to the Centre for Information Services and High Performance Computing [Zentrum für Informationsdienste und Hochleistungsrechnen (ZIH)] TU Dresden for providing its facilities for high throughput calculations.

CRediT authorship contribution statement

Paul Seibert: Conceptualization, Formal analysis, Investigation, Methodology, Software, Validation, Visualization, Writing - original draft, Writing - review and editing. **Alexander Raßloff:** Conceptualization, Investigation, Methodology, Writing - review and editing. **Karl A. Kalina:** Conceptualization, Methodology, Visualization, Writing - review and editing. **Joachim Gussone:** Resources, Writing - original draft, Writing - review and editing. **Katrin Bugelnig:** Resources, Writing - review and editing. **Martin Diehl:** Software, Writing - review and editing. **Markus Kästner:** Funding acquisition, Resources, Writing - review and editing.

A. Descriptor-based smoothing

The difference between the descriptor-based smoothing suggested in Section 2 and simple Gaussian smoothing followed by thresholding is not very pronounced in the investigated structures. However, this is not always the case. In this section, a simple academic example is constructed to illustrate the differences between the methods. Consider a structure with a horizontal slit as shown in Figure 14 (a), which is to be recovered from a noisy version in Figure 14 (b). This noisy version could, for example, stem from a reconstruction algorithm. As can be seen in Figure 14 (c), simple Gaussian smoothing followed by thresholding fails to differentiate between noisy pixels and true sharp corners, hence the smoothing significantly alters the microstructure and its effective properties. In contrast, the suggested descriptor-based smoothing procedure exactly recovers the original structure in very few iterations[10]. In conclusion, although simple smoothing procedures *can* work for real microstructures, there is no warranty that they do. It is therefore recommended to use descriptor-based smoothing procedures whenever possible, despite the higher computational cost.

[10]The number of iterations varies but is mostly less than 10.

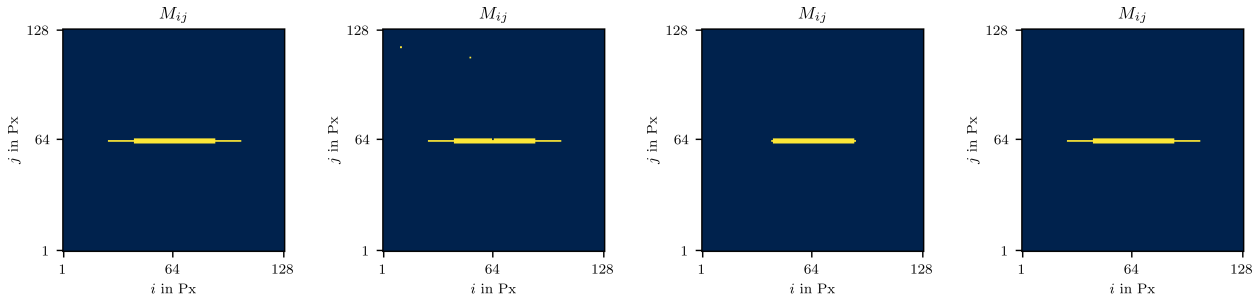

(a) Original structure (b) Noisy version of (a) (c) Standard Gaussian smoothing and thresholding of (b) (d) Suggested descriptor-based smoothing of (b)

Figure 14: Motivation of descriptor-based smoothing: Sharp corners in the original structure (a) cannot be distinguished from noise (b) by a simple Gaussian smoothing and significant errors occur (c). In contrast, the descriptor-based algorithm recovers the original structure (d).

Table 6
The effect of averaging descriptors over multiple slices on the effective Young's modulus under tension in $\boldsymbol{x}$-direction compared to a larger single slice. The $\boldsymbol{y}$- and $\boldsymbol{z}$-direction are similar

$\mathcal{E}_{\overline{E}_x}$	Columnar	Lamellar
Small sample, single slice	−7.8%	−11%
Small sample, averaged slices	−0.5%	−8.4%
Large sample, single slice	−2.1%	−2.0%

B. Size of original slice

If the original 2D microscopy image or slice for the computation of the desired descriptor in Eq. (6) is small, then, as discussed in Section 4.2, the descriptor is most likely not representative for the entire structure. For example, in a matrix structure with inclusions, as the sample size decreases, if becomes increasingly likely that a random 2D slice does not cut a single inclusion. In this extreme case, the result of the characterization would be an inclusion volume fraction of 0%. To demonstrate this effect, a smaller cuboid with 128^3 voxels is cut out of the columnar and lamellar spinodoid structures and used for validation in analogy to Figure 1. Figure 15 summarizes the error in the effective elastic and plastic properties. In direct comparison to the results from the full original structure in Figure 13, a significantly increased scatter can be observed as well as a larger error in general. In theory, for increasing the representativeness of a descriptor, averaging descriptors over multiple slices of a small sample should have the same effect as using a single slice of a larger sample. This is, however, less relevant in practice, since as discussed in the introduction, 3D data is often significantly more cost- and time-intensive to obtain than 2D data. Nevertheless, the authors averaged the descriptor over all slices from the smaller version of the original structure and used this value for an additional reconstruction and homogenization. To keep the computational effort for this a simple experiment low, only a single example was reconstructed in this manner. Indeed, averaging descriptors over multiple small slices has a similar effect as using a single large slice as can be seen in Table 6. This shows the possibility to use multiple 2D microscopy images if this is of interest.

C. Effect of smoothing

The impact of smoothing on the effective properties is outlined in Table 7, where the unsmoothed and smoothed version of the same reconstructed structure are compared regarding their effective properties. In general, a lower stiffness is observed for unsmoothed structures. This can be explained as follows. Consider a connected domain of the stiffer phase. Random noise has the effect of erroneously assigning the weaker phase to some voxels within that domain, thus weakening its effective stiffness. On the other side, in a connected domain of the more compliant phase, single voxels with higher stiffness do not contribute much to the overall behavior as long as they are not connected.

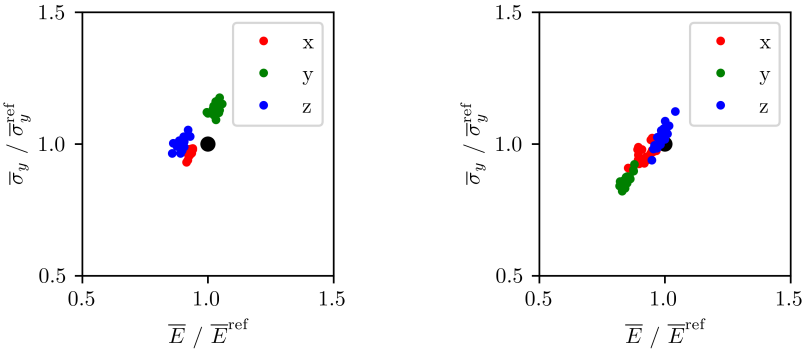

(a) Columnar structure (b) Lamellar structure

Figure 15: Relative error of the effective directional Young's modulus and yield strength for the spinodoid structures when using an insufficiently-sized structure for computing the desired descriptor. Compared to Figure 13, a higher scatter is observed and the error is larger in general.

Table 7
Effect of smoothing on the effective Young's modulus and shear stress for the spinodoid structures.

	$\mathcal{E}_{\overline{E}}$		$\mathcal{E}_{\overline{\sigma}_y}$	
	unsmoothed	smoothed	unsmoothed	smoothed
Columnar	−1.3%	0.1%	−0.9%	0.5%
Lamellar	−4.1%	−2.0%	−1.9%	−0.3%

Similarly, spurious noise acts as a stress concentrator and thus promotes strain localization at lower stress levels. Hence, it is plausible that smoothing increases the effective yield strength. An even larger impact is expected to occur if fatigue indicator parameters are to be computed as in [48], which further underlines the need for microstructure post-processing.

References

[1] Adam, A., Wang, F., Li, X., 2022. Efficient reconstruction and validation of heterogeneous microstructures for energy applications. International Journal of Energy Research , er.8578URL: https://onlinelibrary.wiley.com/doi/10.1002/er.8578, doi:10.1002/er.8578.

[2] Bargmann, S., Klusemann, B., Markmann, J., Schnabel, J.E., Schneider, K., Soyarslan, C., Wilmers, J., 2018. Generation of 3d representative volume elements for heterogeneous materials: A review. Progress in Materials Science 96, 322–384. URL: https://linkinghub.elsevier.com/retrieve/pii/S0079642518300161, doi:10.1016/j.pmatsci.2018.02.003.

[3] Basista, M., Węglewski, W., Bochenek, K., Poniżnik, Z., Nowak, Z., 2017. Micro-CT finite element analysis of thermal residual stresses and fracture in metal-ceramic composites: Micro-CT finite element analysis.... Advanced Engineering Materials 19, 1600725. URL: https://onlinelibrary.wiley.com/doi/10.1002/adem.201600725, doi:10.1002/adem.201600725.

[4] Bostanabad, R., 2020-11. Reconstruction of 3d microstructures from 2d images via transfer learning. Computer-Aided Design 128, 102906. doi:10.1016/j.cad.2020.102906.

[5] Bostanabad, R., Zhang, Y., Li, X., Kearney, T., Brinson, L.C., Apley, D.W., Liu, W.K., Chen, W., 2018. Computational microstructure characterization and reconstruction: Review of the state-of-the-art techniques. Progress in Materials Science 95, 1–41. doi:10.1016/j.pmatsci.2018.01.005.

[6] Brough, D.B., Wheeler, D., Kalidindi, S.R., 2017. Materials knowledge systems in python—a data science framework for accelerated development of hierarchical materials. Integrating Materials and Manufacturing Innovation 6, 36–53. doi:10.1007/s40192-017-0089-0.

[7] Byrd, R.H., Hansen, S.L., Nocedal, J., Singer, Y., 2015. A stochastic quasi-newton method for large-scale optimization. arXiv:1401.7020 [cs, math, stat] URL: http://arxiv.org/abs/1401.7020, arXiv:1401.7020.

[8] Böhlke, T., Brüggemann, C., 2001. Graphical representation of the generalized hooke's law. Technische Mechanik 21, 145–158.

[9] Chandrasekhar, A., Sridhara, S., Suresh, K., 2021. Integrating material selection with design optimization via neural networks. URL: http://arxiv.org/abs/2112.12566, arXiv:2112.12566 [cs].

[10] Diehl, M., Naunheim, Y., Yan, D., Morsdorf, L., An, D., Tasan, C.C., Zaefferer, S., Roters, F., Raabe, D., 2017. Coupled experimental-numerical analysis of strain partitioning in metallic microstructures: The importance of considering the 3d morphology .

[11] Diehl, M., Shanthraj, P., Eisenlohr, P., Roters, F., 2016. Neighborhood influences on stress and strain partitioning in dual-phase microstructures: An investigation on synthetic polycrystals with a robust spectral-based numerical method 51, 429–441. URL: http://link.springer.com/10.1007/s11012-015-0281-2, doi:10.1007/s11012-015-0281-2.

[12] Dueck, G., 1993. New optimization heuristics. Journal of Computational Physics 104, 86–92.

[13] Eidel, B., 2022. Deep CNNs as universal predictors of elasticity tensors in homogenization. CMAME 403, 28. doi:https://doi.org/10.1016/j.cma.2022.115741.

[14] ESRF, 2023. ID16A - Nano-imaging Beamline. URL: https://www.esrf.fr/UsersAndScience/Experiments/XNP/ID16A. last Modified: Mon, 19 Jul 2021 15:58:19 GMT.

[15] Fan, L., Zhang, F., Fan, H., Zhang, C., 2019. Brief review of image denoising techniques. Visual Computing for Industry, Biomedicine, and Art 2, 7. URL: https://vciba.springeropen.com/articles/10.1186/s42492-019-0016-7, doi:10.1186/s42492-019-0016-7.

[16] Fuhg, J.N., Böhm, C., Bouklas, N., Fau, A., Wriggers, P., Marino, M., 2021. Model-data-driven constitutive responses: Application to a multiscale computational framework. International Journal of Engineering Science 167, 103522. URL: https://www.sciencedirect.com/science/article/pii/S0020722521000690, doi:10.1016/j.ijengsci.2021.103522.

[17] Gajek, S., Schneider, M., Böhlke, T., 2022. An FE-DMN method for the multiscale analysis of thermomechanical composites. Computational Mechanics 69, 1087–1113. URL: https://link.springer.com/10.1007/s00466-021-02131-0, doi:10.1007/s00466-021-02131-0.

[18] Gebhardt, U., Schulz, P., Raßloff, A., Koch, I., Gude, M., Kästner, M., 2022. Influence of CT image processing on the predicted impact of pores on fatigue of additively manufactured ti6al4v and AlSi10mg. GAMM-Mitteilungen URL: https://onlinelibrary.wiley.com/doi/10.1002/gamm.202200017, doi:10.1002/gamm.202200017.

[19] Geers, M., Kouznetsova, V., Brekelmans, W., 2010. Multi-scale computational homogenization: Trends and challenges 234, 2175–2182. URL: https://linkinghub.elsevier.com/retrieve/pii/S0377042709005536, doi:10.1016/j.cam.2009.08.077.

[20] Groeber, M.A., Jackson, M.A., 2014. DREAM.3d: A digital representation environment for the analysis of microstructure in 3d. Integrating Materials and Manufacturing Innovation 3, 56–72. doi:10.1186/2193-9772-3-5.

[21] Gussone, J., Bugelnig, K., Barriobero-Vila, P., da Silva, J.C., Hecht, U., Dresbach, C., Sket, F., Cloetens, P., Stark, A., Schell, N., Haubrich, J., Requena, G., 2020. Ultrafine eutectic ti-fe-based alloys processed by additive manufacturing – a new candidate for high temperature applications. Applied Materials Today 20, 100767. URL: https://linkinghub.elsevier.com/retrieve/pii/S2352940720302158, doi:10.1016/j.apmt.2020.100767.

[22] Habraken, A.M., Aksen, T.A., Alves, J.L., Amaral, R.L., Betaieb, E., Chandola, N., Corallo, L., Cruz, D.J., Duchêne, L., Engel, B., Esener, E., Firat, M., Frohn-Sörensen, P., Galán-López, J., Ghiabakloo, H., Kestens, L.A.I., Lian, J., Lingam, R., Liu, W., Ma, J., Menezes, L.F., Nguyen-Minh, T., Miranda, S.S., Neto, D.M., Pereira, A.F.G., Prates, P.A., Reuter, J., Revil-Baudard, B., Rojas-Ulloa, C., Sener, B., Shen, F., Van Bael, A., Verleysen, P., Barlat, F., Cazacu, O., Kuwabara, T., Lopes, A., Oliveira, M.C., Santos, A.D., Vincze, G., 2022. Analysis of ESAFORM 2021 cup drawing benchmark of an al alloy, critical factors for accuracy and efficiency of FE simulations 15, 61. URL: https://link.springer.com/10.1007/s12289-022-01672-w, doi:10.1007/s12289-022-01672-w.

[23] Henkes, A., Caylak, I., Mahnken, R., 2021. A deep learning driven pseudospectral PCE based FFT homogenization algorithm for complex microstructures. Computer Methods in Applied Mechanics and Engineering 385, 114070. URL: https://www.sciencedirect.com/science/article/pii/S0045782521004011, doi:10.1016/j.cma.2021.114070.

[24] Henkes, A., Wessels, H., 2022. Three-dimensional microstructure generation using generative adversarial neural networks in the context of continuum micromechanics. Computer Methods in Applied Mechanics and Engineering 400, 115497. URL: https://linkinghub.elsevier.com/retrieve/pii/S0045782522005126, doi:10.1016/j.cma.2022.115497.

[25] Hsieh, M.T., Endo, B., Zhang, Y., Bauer, J., Valdevit, L., 2019. The mechanical response of cellular materials with spinodal topologies. Journal of the Mechanics and Physics of Solids 125, 401–419. URL: https://www.sciencedirect.com/science/article/pii/S0022509618307750, doi:10.1016/j.jmps.2019.01.002.

[26] Jiao, Y., Stillinger, F.H., Torquato, S., 2007. Modeling heterogeneous materials via two-point correlation functions: Basic principles. Physical Review E 76, 031110. doi:10.1103/PhysRevE.76.031110.

[27] Kabel, M., Merkert, D., Schneider, M., 2015. Use of composite voxels in FFT-based homogenization. Computer Methods in Applied Mechanics and Engineering 294, 168–188. URL: https://linkinghub.elsevier.com/retrieve/pii/S0045782515001954, doi:10.1016/j.cma.2015.06.003.

[28] Kalina, K.A., Linden, L., Brummund, J., Kästner, M., 2022. FEANN – an efficient data-driven multiscale approach based on physics-constrained neural networks and automated data mining. ArXiv , 21.

[29] Karsanina, M.V., Gerke, K.M., 2018. Hierarchical optimization: Fast and robust multiscale stochastic reconstructions with rescaled correlation functions 121, 265501. URL: https://link.aps.org/doi/10.1103/PhysRevLett.121.265501, doi:10.1103/PhysRevLett.121.265501.

[30] Kench, S., Cooper, S.J., 2021. Generating 3d structures from a 2d slice with GAN-based dimensionality expansion. Nat Mach Intell 3, 299–305. doi:https://doi.org/10.1038/s42256-021-00322-1, arXiv:2102.07708.

[31] Keshav, S., Fritzen, F., Kabel, M., 2022. FFT-based homogenization at finite strains using composite boxels (ComBo). arXiv:2204.13624 [cs, math] URL: http://arxiv.org/abs/2204.13624, arXiv:2204.13624.

[32] Kraska, M., Doig, M., Tikhomirov, D., Raabe, D., Roters, F., 2009. Virtual material testing for stamping simulations based on polycrystal plasticity 46, 383–392. URL: https://linkinghub.elsevier.com/retrieve/pii/S0927025609001256, doi:10.1016/j.commatsci.2009.03.025.

[33] Kumar, S., Tan, S., Zheng, L., Kochmann, D.M., 2020. Inverse-designed spinodoid metamaterials. npj Computational Materials 6, 73. URL: http://www.nature.com/articles/s41524-020-0341-6, doi:10.1038/s41524-020-0341-6.

[34] Le, B.A., Yvonnet, J., He, Q.C., 2015. Computational homogenization of nonlinear elastic materials using neural networks. International Journal for Numerical Methods in Engineering 104, 1061–1084. URL: https://onlinelibrary.wiley.com/doi/abs/10.1002/nme.

4953, doi:10.1002/nme.4953. _eprint: https://onlinelibrary.wiley.com/doi/pdf/10.1002/nme.4953.

[35] Li, B., Zhuang, X., 2020. Multiscale computation on feedforward neural network and recurrent neural network. Frontiers of Structural and Civil Engineering 14, 1285–1298. URL: https://link.springer.com/10.1007/s11709-020-0691-7, doi:10.1007/s11709-020-0691-7.

[36] Li, X., Yang, Z., Brinson, L.C., Choudhary, A., Agrawal, A., Chen, W., 2018. A deep adversarial learning methodology for designing microstructural material systems, in: Volume 2B: 44th Design Automation Conference, American Society of Mechanical Engineers. p. V02BT03A008. doi:10.1115/DETC2018-85633.

[37] Liu, Z., Wu, C.T., 2019. Exploring the 3d architectures of deep material network in data-driven multiscale mechanics. Journal of the Mechanics and Physics of Solids 127, 20–46. URL: https://www.sciencedirect.com/science/article/pii/S0022509618310688, doi:10.1016/j.jmps.2019.03.004.

[38] Liu, Z., Wu, C.T., Koishi, M., 2019. A deep material network for multiscale topology learning and accelerated nonlinear modeling of heterogeneous materials. Computer Methods in Applied Mechanics and Engineering 345, 1138–1168. URL: https://www.sciencedirect.com/science/article/pii/S0045782518304729, doi:10.1016/j.cma.2018.09.020.

[39] Lubbers, N., Lookman, T., Barros, K., 2017. Inferring low-dimensional microstructure representations using convolutional neural networks. Phys. Rev. E 96, 052111. URL: https://link.aps.org/doi/10.1103/PhysRevE.96.052111, doi:10.1103/PhysRevE.96.052111.

[40] Masi, F., Stefanou, I., 2022. Multiscale modeling of inelastic materials with thermodynamics-based artificial neural networks (TANN). Computer Methods in Applied Mechanics and Engineering 398, 115190. URL: http://arxiv.org/abs/2108.13137, doi:10.1016/j.cma.2022.115190, arXiv:2108.13137 [cond-mat, physics:physics].

[41] Moerman, K.M., 2018. GIBBON: The geometry and image-based bioengineering add-on. Journal of Open Source Software 3, 506. URL: https://joss.theoj.org/papers/10.21105/joss.00506, doi:10.21105/joss.00506.

[42] Moulinec, H., Suquet, P., 1998. A numerical method for computing the overall response of nonlinear composites with complex microstructure 157, 69–94. URL: http://arxiv.org/abs/2012.08962, doi:10.1016/S0045-7825(97)00218-1, arXiv:2012.08962 [physics].

[43] do Nascimento, A.W.P., Roongta, S., Diehl, M., Beyerlein, I.J., 2022. A machine learning model to predict yield surfaces from crystal plasticity simulations , 103507URL: https://www.sciencedirect.com/science/article/pii/S0749641922002844, doi:10.1016/j.ijplas.2022.103507.

[44] Nordmann, J., Aßmus, M., Altenbach, H., 2018. Visualising elastic anisotropy: theoretical background and computational implementation. Continuum Mechanics and Thermodynamics 30, 689–708. URL: http://link.springer.com/10.1007/s00161-018-0635-9, doi:10.1007/s00161-018-0635-9.

[45] Pant, L.M., Mitra, S.K., Secanell, M., 2014. Stochastic reconstruction using multiple correlation functions with different-phase-neighbor-based pixel selection. Physical Review E 90, 023306. doi:10.1103/PhysRevE.90.023306.

[46] Pant, L.M., Mitra, S.K., Secanell, M., 2015. Multigrid hierarchical simulated annealing method for reconstructing heterogeneous media 92, 063303. URL: https://link.aps.org/doi/10.1103/PhysRevE.92.063303, doi:10.1103/PhysRevE.92.063303.

[47] Phan, J., Ruspini, L., Kiss, G., Lindseth, F., 2022. Size-invariant 3d generation from a single 2d rock image. Journal of Petroleum Science and Engineering , 9.

[48] Raßloff, A., Schulz, P., Kühne, R., Ambati, M., Koch, I., Gude, M., Zimmermann, M., Kästner, M., 2021. Accessing pore microstructure-property relationships for additively manufactured materials. GAMM Mitteilungen , 1–21.

[49] Roters, F., Diehl, M., Shanthraj, P., Eisenlohr, P., Reuber, C., Wong, S., Maiti, T., Ebrahimi, A., Hochrainer, T., Fabritius, H.O., Nikolov, S., Friák, M., Fujita, N., Grilli, N., Janssens, K., Jia, N., Kok, P., Ma, D., Meier, F., Werner, E., Stricker, M., Weygand, D., Raabe, D., 2019. DAMASK – the düsseldorf advanced material simulation kit for modeling multi-physics crystal plasticity, thermal, and damage phenomena from the single crystal up to the component scale. Computational Materials Science 158, 420–478. doi:10.1016/j.commatsci.2018.04.030.

[50] Sahimi, M., Tahmasebi, P., 2021. Reconstruction, optimization, and design of heterogeneous materials and media: Basic principles, computational algorithms, and applications. Physics Reports 939, 1–82. URL: https://linkinghub.elsevier.com/retrieve/pii/S0370157321003719, doi:10.1016/j.physrep.2021.09.003.

[51] Scheunemann, L., Balzani, D., Brands, D., Schröder, J., 2015. Design of 3d statistically similar representative volume elements based on minkowski functionals. Mechanics of Materials 90, 185–201. doi:10.1016/j.mechmat.2015.03.005.

[52] Schlieter, A., Kühn, U., Eckert, J., Löser, W., Gemming, T., Friák, M., Neugebauer, J., 2011. Anisotropic mechanical behavior of ultrafine eutectic TiFe cast under non-equilibrium conditions. Intermetallics 19, 327–335. URL: https://linkinghub.elsevier.com/retrieve/pii/S0966979510004280, doi:10.1016/j.intermet.2010.10.012.

[53] Schneider, C.A., Rasband, W.S., Eliceiri, K.W., 2012. NIH image to ImageJ: 25 years of image analysis. Nature Methods 9, 671–675. URL: http://www.nature.com/articles/nmeth.2089, doi:10.1038/nmeth.2089.

[54] Schneider, M., 2015. Convergence of FFT-based homogenization for strongly heterogeneous media. Mathematical Methods in the Applied Sciences 38, 2761–2778. URL: https://onlinelibrary.wiley.com/doi/10.1002/mma.3259, doi:10.1002/mma.3259.

[55] Schneider, M., 2021. A review of nonlinear FFT-based computational homogenization methods. Acta Mechanica 232, 2051–2100. URL: https://link.springer.com/10.1007/s00707-021-02962-1, doi:10.1007/s00707-021-02962-1.

[56] Seibert, P., Ambati, M., Raßloff, A., Kästner, M., 2021. Reconstructing random heterogeneous media through differentiable optimization. Computational Materials Science , 16.

[57] Seibert, P., Raßloff, A., Ambati, M., Kästner, M., 2022a. Descriptor-based reconstruction of three-dimensional microstructures through gradient-based optimization. Acta Materialia 227, 117667. URL: https://linkinghub.elsevier.com/retrieve/pii/S1359645422000520, doi:10.1016/j.actamat.2022.117667.

[58] Seibert, P., Raßloff, A., Kalina, K., Ambati, M., Kästner, M., 2022b. Microstructure characterization and reconstruction in python: MCRpy. IMMJ , 14.

[59] Simonyan, K., Zisserman, A., 2015. Very deep convolutional networks for large-scale image recognition. CoRR abs/1409.1556.

[60] Wessels, H., Böhm, C., Aldakheel, F., Hüpgen, M., Haist, M., Lohaus, L., Wriggers, P., 2022. Computational homogenization using convolutional neural networks, in: Aldakheel, F., Hudobivnik, B., Soleimani, M., Wessels, H., Weißenfels, C., Marino, M. (Eds.), Current Trends and Open Problems in Computational Mechanics. Springer International Publishing, pp. 569–579. URL: https://doi.org/10.1007/978-3-030-87312-7_55, doi:10.1007/978-3-030-87312-7_55.

[61] Xu, H., Li, Y., Brinson, C., Chen, W., 2014. A descriptor-based design methodology for developing heterogeneous microstructural materials system. Journal of Mechanical Design 136. URL: https://asmedigitalcollection.asme.org/mechanicaldesign/article/136/5/051007/375780/A-Descriptor-Based-Design-Methodology-for, doi:10.1115/1.4026649.

[62] Yeong, C.L.Y., Torquato, S., 1998. Reconstructing random media. Physical Review E 57, 495–506. doi:10.1103/PhysRevE.57.495.

[63] Zeghadi, A., Forest, S., Gourgues, A.F., Bouaziz, O., 2007a. Ensemble averaging stress–strain fields in polycrystalline aggregates with a constrained surface microstructure – part 2: crystal plasticity 87, 1425–1446. URL: http://www.tandfonline.com/doi/abs/10.1080/14786430601009517, doi:10.1080/14786430601009517.

[64] Zeghadi, A., N'guyen, F., Forest, S., Gourgues, A.F., Bouaziz, O., 2007b. Ensemble averaging stress–strain fields in polycrystalline aggregates with a constrained surface microstructure – part 1: anisotropic elastic behaviour 87, 1401–1424. URL: http://www.tandfonline.com/doi/abs/10.1080/14786430601009509, doi:10.1080/14786430601009509.

[65] Zhang, F., Teng, Q., Chen, H., He, X., Dong, X., 2021. Slice-to-voxel stochastic reconstructions on porous media with hybrid deep generative model. Computational Materials Science 186, 110018. doi:10.1016/j.commatsci.2020.110018.

[66] Zhang, H., Diehl, M., Roters, F., Raabe, D., 2016. A virtual laboratory using high resolution crystal plasticity simulations to determine the initial yield surface for sheet metal forming operations 80, 111–138. URL: https://linkinghub.elsevier.com/retrieve/pii/S0749641916000036, doi:10.1016/j.ijplas.2016.01.002.

[67] Zhao, X., Yao, J., Yi, Y., 2007. A new stochastic method of reconstructing porous media. Transport in Porous Media 69, 1–11. doi:10.1007/s11242-006-9052-9.

[68] Zheng, L., Kumar, S., Kochmann, D.M., 2021. Data-driven topology optimization of spinodoid metamaterials with seamlessly tunable anisotropy. Computer Methods in Applied Mechanics and Engineering 383, 113894. URL: https://linkinghub.elsevier.com/retrieve/pii/S0045782521002310, doi:10.1016/j.cma.2021.113894.

[69] Zhu, L.F., Friák, M., Dick, A., Grabowski, B., Hickel, T., Liot, F., Holec, D., Schlieter, A., Kühn, U., Eckert, J., Ebrahimi, Z., Emmerich, H., Neugebauer, J., 2012. First-principles study of the thermodynamic and elastic properties of eutectic fe–ti alloys. Acta Materialia 60, 1594–1602. URL: https://linkinghub.elsevier.com/retrieve/pii/S1359645411008366, doi:10.1016/j.actamat.2011.11.046.

[70] Zhu, L.F., Friák, M., Udyansky, A., Ma, D., Schlieter, A., Kühn, U., Eckert, J., Neugebauer, J., 2014. Ab initio based study of finite-temperature structural, elastic and thermodynamic properties of FeTi. Intermetallics 45, 11–17. URL: https://linkinghub.elsevier.com/retrieve/pii/S0966979513002495, doi:10.1016/j.intermet.2013.09.008.